



---

19 **Abstract**

20 Rapid decline of Arctic sea ice has created more open water for ocean wave development  
21 and highlighted the importance of wave-ice interactions in the Arctic. Some studies have made  
22 contributions to our understanding of the potential role of the prognostic floe size distribution  
23 (FSD) on sea ice changes. However, these efforts do not represent the full interactions across  
24 atmosphere, ocean, wave, and sea-ice. In this study, we implement a modified joint floe size  
25 and thickness distribution (FSTD) in a newly-developed regional atmosphere-ocean-wave-sea  
26 ice coupled model and conduct a series of pan-Arctic simulation with different physical  
27 configurations related to FSD changes, including FSD-fixed, FSD-varied, lateral melting rate,  
28 wave-fracturing formulation, and wave attenuation rate. Firstly, our atmosphere-ocean-wave-  
29 sea ice coupled simulations show that the prognostic FSD leads to reduced ice area due to  
30 enhanced ice-ocean heat fluxes, but the feedbacks from the atmosphere and the ocean partially  
31 offset the reduced ice area induced by the prognostic FSD. Secondly, lateral melting rate  
32 formulations do not change the simulated FSD significantly, but they influence the flux  
33 exchanges across atmosphere, ocean, and sea-ice and thus sea ice responses. Thirdly, the  
34 changes of FSD are sensitive to the simulated wave height, wavelength, and wave period  
35 associated with different wave-fracturing formulations and wave attenuation rates, and the  
36 limited oceanic energy imposes a strong constraint on the response of sea ice to FSD changes.  
37 Finally, our results also demonstrate that wave-related physical processes can have impacts on  
38 sea ice changes with the constant FSD, suggesting the indirect influences of ocean waves on  
39 sea-ice through the atmosphere and the ocean.

删除了: for

---

## 41 1. Introduction

42 Arctic sea ice, a major component in the climate system, has undergone dramatic changes  
43 over the past few decades associated with global climate change. September and March Arctic  
44 sea ice extent show decreasing trends of -13.1% and -2.6% per decade from 1979 to 2020,  
45 respectively (Perovich et al., 2020). The mean Arctic sea ice thickness has decreased by ~1.5-  
46 2 meters from the submarine period (1958-1976) to the satellite period (2011-2018), largely  
47 resulting from the loss of multiyear ice (Kwok, 2018; Tschudi et al., 2016). The drifting speed  
48 of Arctic sea ice exhibits an increasing trend based on satellite and buoy observations (e.g.,  
49 Rampal et al., 2009; Spreen et al., 2011; Zhang et al., 2022). As the Arctic Ocean has been  
50 dominated by thinner and younger ice, Arctic sea ice is more likely to be influenced by forcings  
51 from the atmosphere and the ocean.

52 Associated with the above Arctic sea ice changes, the Arctic fetch (open water area for  
53 ocean wave development) is less limited by the ice cover. The increased Arctic fetch and  
54 surface wind speed can lead to higher ocean waves in the Arctic Ocean based on observations,  
55 reanalysis, and future projections (Casas-Prat and Wang, 2020; Dobrynin et al., 2012; Liu et  
56 al., 2016; Stopa et al., 2016; Waseda et al., 2018). The higher ocean waves are more likely to  
57 propagate deeper into the ice pack and have sufficient energy to break sea ice into smaller floes  
58 (e.g., Kohout et al., 2014). Sea ice with mostly smaller floes has larger surface areas,  
59 particularly lateral surfaces. The increased lateral surface accelerates ice melting through  
60 enhanced ice-ocean heat fluxes (e.g., Steele, 1992). Some studies also showed that the ice-floe  
61 melting rate is associated with the horizontal mixing of oceanic heat across ice floe edge

删除了: shows

删除了: dominating

删除了: are able to

删除了: area

删除了: surface

删除了: a result of the interaction between floe size and ocean circulation

69 between open water and under-floe ocean by oceanic eddies, in particular sub-mesoscale eddies,  
70 and the strength of this effect depends on floe size (Gupta and Thompson, 2022; Horvat et al.,  
71 2016). The enhanced ice melting creates more open water (i.e., fetch), which is a favorable  
72 condition for further wave development as well as the ice-albedo feedback (Curry et al., 1995).  
73 These processes create a potential feedback loop between ocean waves and sea ice (e.g., Asplin  
74 et al., 2014; Thomson and Rogers, 2014).

75 Arctic cyclones and their high surface wind are the important drivers for large wave events  
76 in the Arctic Ocean. Previous studies showed that intense storms like the “Great Arctic Cyclone”  
77 of 2012 (Simmonds and Rudeva, 2012) and a strong summer cyclone in 2016 could be one of  
78 the contributors to the anomalously low sea ice extent in 2012 and 2016 (e.g., Lukovich et al.,  
79 2021; Parkinson and Comiso, 2013; Peng et al., 2021; Stern et al., 2020; Zhang et al., 2013).  
80 Statistical analyses based on cyclone-tracking algorithm across multiple reanalyses suggested  
81 that the number of Arctic cyclones shows a significantly positive trend in the cold season (e.g.,  
82 Sepp and Jaagus, 2011; Valkonen et al., 2021; Zahn et al., 2018). The increased cyclone  
83 activities and more open water areas cause more extreme wave events in the Arctic (e.g.,  
84 Waseda et al., 2021). Blanchard-Wrigglesworth et al. (2021) found that extreme changes in  
85 Arctic sea ice extent are correlated with distinct wave conditions during the cold season based  
86 on the observations.

87 The potential feedback loop associated with ocean waves and sea ice and more extreme  
88 wave events indicates the importance of representing these processes in climate models for  
89 improving sea ice simulation and prediction (e.g., Collins et al., 2015; Kohout et al., 2014).

删除了: driver

删除了: contribute

删除了: show

删除了: indicate

删除了: to represent

---

95 However, state-of-the-art climate models participating in the latest Coupled Model  
96 Intercomparison Project Phase 6 (CMIP6) have not incorporated the interactions between  
97 ocean waves and sea ice in their model physics (e.g., Horvat, 2021). The coupled effects of  
98 ocean waves and sea ice include; the amplitude of ocean waves decays as the waves travel  
99 under the ice cover due to the combination of scattering and dissipation (e.g., Squire, 2020).  
100 Crests and troughs of ocean waves exert strains on sea ice, and sea ice breaks if the maximum  
101 strain exceeds a certain threshold (e.g., Dumont et al., 2011). The wave-induced ice-breaking  
102 changes the size of floes, which in turn changes the floe size distribution (FSD; Rothrock and  
103 Thorndike, 1984). In addition to the interactions between ocean waves and sea ice, the floe size  
104 contributes to the changes in the atmospheric boundary layer (e.g., Schäfer et al., 2015; Wenta  
105 and Herman, 2019), mechanical responses of sea ice (e.g., Vella and Wettauer, 2008; Weiss  
106 and Dansereau, 2017; Wilchinsky et al., 2010), the flux exchanges across air-sea ice-ocean  
107 interfaces (Cole et al., 2017; Loose et al., 2014; Lu et al., 2011; Martin et al., 2016; Steele et  
108 al., 1989; Tsamados et al., 2014), and the scattering of ocean wave propagation (e.g., Montiel  
109 et al., 2016; Squire and Montiel, 2016). Thus, it is essential to have a prognostic FSD to  
110 properly reflect wave-ice interactions as well as other processes related to the floe size in  
111 climate models.

112 Recently, several studies have made contributions on understating responses of sea ice to  
113 the prognostic FSD (e.g., Bateson et al., 2020; Bennetts et al., 2017; Boutin et al., 2020; Horvat  
114 and Tziperman, 2015; Roach et al., 2018a, 2019; Zhang et al., 2015, 2016). However, these  
115 studies used simplified model complexity (i.e., standalone sea ice model, ice-wave coupling,

删除了: to

删除了:

删除了: of

删除了: Schafer

120 ice-ocean coupling) and were unable to give a full representation of sea ice responses to the  
121 evolving states of atmosphere, ocean, and wave, based on explicit model physics as well as  
122 feedbacks from sea ice to them. Motivated by this, here we introduce a newly-developed  
123 atmosphere-ocean-wave-sea ice coupled model, in which we implement physical processes  
124 that simulate the evolution of floe size distribution. We use this new coupled model to  
125 investigate the responses of sea ice to ocean waves, as well as interactions in the Arctic climate  
126 system. This paper is structured as follows. Section 2 provides an overview of the new coupled  
127 model, focusing on the wave component and the implementation of the prognostic FSD.  
128 Section 3 describes the design of numerical experiments and the related model configurations.  
129 Section 4 examines the responses of sea ice to wave-ice interactions with the prognostic FSD,  
130 as well as other ocean wave-related processes. Discussions and concluding remarks are  
131 provided in section 5.

删除了: under

删除了: interactions across

删除了: , and

删除了: waves

## 133 2. Model description

134 The newly-developed atmosphere-ocean-wave-sea ice coupled model is based on  
135 Coupled Arctic Prediction System (CAPS, Yang et al., 2022), which consists of the Weather  
136 Research and Forecasting Model (WRF), the Regional Ocean Modeling System (ROMS), and  
137 the Community Ice Code (CICE). The detailed description of each model component in CAPS  
138 is referred to Yang et al. (2020; 2022). In this section, we focus on newly-added features in  
139 CAPS as described below.

### 140 2.1. Wave model component

145 To represent wave-ice interactions, an ocean wave model is coupled into CAPS, which is  
 146 the Simulating Waves Nearshore (SWAN). SWAN is a third-generation wave model and  
 147 includes processes of diffraction, refraction, wave-wave interactions, and wave dissipation due  
 148 to wave breaking, whitecapping, and bottom friction (Booij et al., 1999). Recently, the SWAN  
 149 model has implemented wave dissipation due to sea ice based on an empirical formula, which  
 150 is called IC4M2 (Collins and Rogers, 2017; Rogers, 2019). Specifically, the temporal  
 151 exponential decay rate of wave energy due to sea ice is defined as,

$$154 \quad S_{ice}/E = -2c_g k_i \quad (1)$$

152 where  $S_{ice}$  is the sink term induced by sea ice,  $E$  is the wave energy spectrum, and  $c_g$  is the  
 153 group velocity.  $k_i$  is the linear exponential rate that is a function of frequency as follow,

$$158 \quad k_i(f) = c_0 + c_1 f + c_2 f^2 + c_3 f^3 + c_4 f^4 + c_5 f^5 + c_6 f^6 \quad (2)$$

155 where  $c_0$  to  $c_6$  are the user-defined coefficients and their values as described in Section 3. In  
 156 the SWAN model, both the wind source term  $S_{in}$ , and the sea ice sink term are scaled by sea  
 157 ice concentration  $a_{ice}$ , which is provided by the CICE model through the coupler in CAPS,

$$159 \quad S_{ice} \rightarrow a_{ice} S_{ice} \quad (3)$$

$$160 \quad S_{in} \rightarrow (1 - a_{ice}) S_{in} \quad (4)$$

## 161 2.2. Prognostic FSD

162 For the prognostic FSD implemented in the CICE model, we follow the joint floe size and  
 163 thickness distribution (FSTD; Horvat and Tziperman, 2015). The FSTD is defined as a  
 164 probability distribution  $f(r, h) dr dh$ .  $f(r, h)$  represents the fraction of cell covered by ice with  
 165 floe size between  $r$  and  $r + \Delta r$ , thickness between  $h$  and  $h + \Delta h$ , and the FSTD satisfies,

169

$$\int_{\mathcal{R}} \int_{\mathcal{H}} f(r, h) dr dh = 1 \quad (5)$$

166

The ice thickness distribution  $g(h)$  (ITD; Thorndike et al., 1975), which is simulated by the

167

CICE model, and the FSD  $F(r)$ , can be obtained by integrating the FSTD over all floe sizes

168

and all ice thicknesses,

172

$$\begin{aligned} \int_{\mathcal{R}} f(r, h) dr &= g(h) \\ \int_{\mathcal{H}} f(r, h) dh &= F(r) \end{aligned} \quad (6)$$

170

Roach et al. (2018a) suggested the modified FSTD,  $L(r, h)$ , to preserve the governing

171

equations of ITD in the CICE model, which satisfies,

178

$$\int_{\mathcal{R}} L(r, h) dr = 1 \quad (7)$$

173

and

179

$$f(r, h) = g(h) L(r, h) \quad (8)$$

174

As described in Roach et al. (2018a), the implementation of the modified FSTD ignores the

175

two-way relationship between floe size, that is, physical processes associated with FSD

176

changes (i.e.,  $L(r, h)$  changes) are independent across each ice thickness category. The

177

governing equation of FSTD is defined as,

183

$$\frac{\partial f(r, h)}{\partial t} = -\nabla \cdot (f(r, h) \vec{v}) + \mathcal{L}_T + \mathcal{L}_M + \mathcal{L}_W \quad (9)$$

180

The terms on the right-hand side represent advection, thermodynamics, mechanical, and wave-

181

induced floe-fracturing processes. For these terms, except the last term  $\mathcal{L}_W$ , we follow the

182

approach described in Roach et al. (2018a) and related values for coefficients as described in

删除了:

删除了: in

删除了: -



187 Section 3. The formulations of  $\mathcal{L}_W$  proposed by Horvat and Tziperman (2015) involve a  
188 random function to generate sub-grid scale sea surface elevation to determine how floes are  
189 fractured by ocean waves. As a consequence, simulations are not bitwise reproducible with the  
190 formulation including a random function. To avoid this issue, we propose different approaches  
191 for our implementation of FSTD as described below.

删除了: in

删除了: involves

### 192 2.3. Floe fracturing by ocean waves

193 For the floe-fracturing term  $\mathcal{L}_W$ , we follow the formulation suggested by Zhang et al.  
194 (2015), which has similar form as Horvat and Tziperman (2015) and can be described as,

$$200 \quad \mathcal{L}_W = -Q(r) f(r, h) + \int_{\mathcal{R}} \beta(r', r) Q(r') f(r', h) dr' \quad (10)$$

195 The first term on the right-hand side represents the areal fraction reduction due to floe-  
196 fracturing and the second term is the areal fraction gain from other floe size categories that  
197 have floe-fracturing. In equation (10),  $Q(r)$  is the probability that floe-fracturing occurs for  
198 floe size between  $r$  and  $r + \Delta r$ , and  $\beta(r', r)$  is the redistributor that transfers fractured floe  
199 from floe size  $r'$  to  $r$ .  $\mathcal{L}_W$  does not create or destroy ice so it must satisfy,

删除了: in

删除了: -

$$202 \quad \int_{\mathcal{R}} \mathcal{L}_W dr = 0 \quad (11)$$

201 In this study, we propose two different formulations for  $Q(r)$  and  $\beta(r', r)$ .

#### 203 (a) Equally-redistribution

204 We follow the same assumption in Zhang et al. (2015). That is, ice-fracturing by ocean  
205 waves is likely to be a random process and the size of fractured floe does not have favored floe  
206 size based on aerial photographs and satellite images (e.g., Steer et al., 2008; Toyota et al.,

211 2006, 2011). Thus, fractured floe is equally-redistributed into smaller floe sizes. The  
 212 redistributor is defined as,

$$215 \quad \beta(r_1, r_2) = \begin{cases} 1/(c_2 r_1 - c_1 r_1) & \text{if } c_1 r_1 \leq r_2 \leq c_2 r_1 \\ 0 & \text{if } r_2 < c_1 r_1 \text{ or } r_2 > c_2 r_1 \end{cases} \quad (12)$$

213 where  $c_1$  and  $c_2$  are constants that define upper- and lower-bound of floe size redistribution.

214 Details of  $\beta(r', r)$  in this formulation are referred to Zhang et al. (2015).

216 For the probability  $Q(r)$ , Zhang et al. (2015) used a user-defined coefficient to reflect  
 217 wave conditions and determine  $Q(r)$ . Zhang et al. (2016) suggested that the coefficient is a  
 218 function of wind speed, fetch, ITD, and FSD. Since CAPS has a wave component to simulate  
 219 wave conditions, we reformulate  $Q(r)$  to include simulated wave information from the coupler,  
 220 and  $Q(r)$  is defined as,

$$227 \quad Q(r) = c_w H(\varepsilon) \exp \left[ -\alpha \left( \frac{1-r}{r_{max}} \right) \right] \quad (13)$$

221 where  $H(\varepsilon)$  is the Heaviside step function, the exponential function determines the fraction of  
 222 each floe size participating in fracturing, and user-defined coefficients,  $c_w$  and  $\alpha$ , control the  
 223 upper-bound of  $Q(r)$  and the shape of the exponential function. To include wave conditions  
 224 from the SWAN model, we apply the floe-fracturing parameterization suggested by Dumont et  
 225 al. (2011) to calculate the strain induced by ocean waves on ice floes, and use this  
 226 parameterization to define  $H(\varepsilon)$  as,

$$230 \quad H(\varepsilon) = \begin{cases} 1, & \text{if } \varepsilon \geq \varepsilon_c \\ 0, & \text{if } \varepsilon < \varepsilon_c \end{cases} \quad (14)$$

$$231 \quad \varepsilon = \frac{2\pi^2 h_{ice} A_{wave}}{L_{wave}^2} \quad (15)$$

228 where the strain  $\varepsilon$  is proportional to the ice thickness  $h_{ice}$  and the mean amplitude of wave  
 229  $A_{wave}$ , and inversely proportional to the square of the mean surface wavelength  $L_{wave}$ . If the

删除了: an

233 strain exceeds the strain yield limit  $\varepsilon_c$  (see Section 3), floe-fracturing occurs (i.e.,  $H(\varepsilon) = 1$ ).

234 The distribution of wave heights is, in general, a Rayleigh distribution, which allows us to use

235 the simulated significant wave height from the SWAN model to determine the mean wave

236 amplitude with the following relationship (e.g., Bai and Bai, 2014),

238 
$$A_{wave} = \frac{H_{wave}}{2} \cong \frac{5}{16} H_s \quad (16)$$

237 where  $H_{wave}$  is the mean wave height, and  $H_s$  is the significant wave height.

239 The exponential function is built on that the wave strain on ice floes is separated by the  
240 wavelength (e.g., Dumont et al., 2011, their Fig. 4). Floe size smaller than the wavelength is  
241 more likely to move along with ocean waves with little bending (e.g., Meylan and Squire, 1994).

242 That is, the exponential function preferentially has a higher fraction for larger floes.

243 (b) Redistribution based on a semi-empirical wave spectrum

244 As discussed in Dumont et al. (2011, their Fig. 4), fractured floes have a maximum size

245 with half of the surface wavelength. Thus, the wave distribution of different wavelengths in

246 each grid cell allows us to predict floe sizes after fracturing. The sea surface elevation is a result

247 of the superimposition of waves with different periods, amplitudes, and directions in space and

248 time. Empirical wave spectra have been proposed to describe wave conditions with a finite set

249 of parameters. Based on wave observations from a wide variety of locations, Bretschneider

250 (1959) suggested the formulation of wave spectrum, which is used to formulate the

251 redistribution of fractured floe as described below.

252 The Bretschneider wave spectrum is defined as,

删除了: -

删除了: cells

删除了: are

删除了: -

---

259 
$$S_B(T) = \frac{1.25H_s^2 T^5}{8\pi T_p^4} \exp\left[-1.25\left(\frac{T}{T_p}\right)^4\right] \quad (17)$$

257 where  $T_p$  is the peak wave period, and the spectral wave amplitude is defined as (Dumont et  
 258 al., 2011),

262 
$$A(T) = \sqrt{\frac{4\pi S_B(T)}{T}} \quad (18)$$

260 Similar to the distribution of wave height, Bretschneider (1959) found that the distribution of  
 261 wave period is, in general, a Rayleigh distribution and defined as,

266 
$$P(T) = 2.7\left(\frac{T}{T_{ave}}\right)^3 \exp\left[-0.675\left(\frac{T}{T_{ave}}\right)^4\right] \quad (19)$$

263 where  $T_{ave}$  is the mean surface period. With the deep-water surface wave dispersion relation  
 264  $L(T) = gT^2/2\pi$ , the corresponding wave length for each wave period bin can be obtained,  
 265 and the wave-strain distribution can be calculated with the modified equation (15),

269 
$$\varepsilon(T) = \frac{2\pi^2 h_{ice} A(T)}{L(T)^2} \quad (20)$$

267 Combined with the Heaviside step function defined in the equation (14), the probability of floe-  
 268 fracturing for each wave period is obtained,

275 
$$P_f(T) = H(\varepsilon(T))\bar{P}(T) \quad (21)$$

270 where  $\bar{P}(T)$  is the normalized  $P(T)$ . Based on  $P_f(T)$  and the assumption that fractured floes  
 271 have a maximum size with half of the surface wavelength, the redistributor  $\beta(r_1, r_2)$  can be  
 272 obtained based on following criteria: 1) floe size between  $r$  and  $r + \Delta r$  (in radius) must be  
 273 greater than half of wavelength  $L(T)$ , 2) floes fractured by the wavelength  $L(T)$  have the size  
 274 of  $L(T)/2$ , and 3)  $P_f(T)$  represents the fraction of floe with  $r$  and  $r + \Delta r$  transferred to new

276 size with  $r'$  and  $r' + \Delta r$  determined by the criterion (2). The probability  $Q(r)$  is the summation  
277 of  $P_f(T)$  and represents the total fraction of floe participating in wave-fracturing.

### 278 3. Model configurations and experiment designs

279 The ~~WRF, ROMS, SWAN, and CICE models use the same~~ model ~~grid with 320 (440) x-~~  
280 (y-) grid points ~~and ~24km horizontal resolution~~ (Fig. 1). Initial and boundary conditions for  
281 the WRF, ROMS, CICE models are generated from the Climate Forecast System version 2  
282 (CFSv2, Saha et al., 2014) operational analysis, archived by National Centers for  
283 Environmental Information (NCEI), National Oceanic and Atmospheric Administration  
284 (NOAA). In our configurations, the SWAN model starts with the calm wave states (i.e., zero  
285 wave energy in all frequencies). The modified FSTD,  $L(r, h)$ , is initialized based on the power-  
286 law distribution of floe number,  $N(r) \propto r^{-a}$  (e.g., Toyota et al., 2006), with the exponent  $a$  as  
287 2.1 for all grid cells. Physical parameterizations of each model component are mostly identical  
288 to those used in Yang et al. (2022) and summarized in Table 1.

289 Cassano et al. (2011) suggested that the use of a higher model top (10 mb) or applying  
290 spectral nudging in the upper model levels ~~leads~~ to significantly reduced bases in pan-Arctic  
291 atmospheric circulation in the standalone WRF model. Thus, compared with Yang et al. (2022),  
292 we change the model top of the WRF model in CAPS from 50 mb to 10 mb. With coupling to  
293 the SWAN model in CAPS, the corresponding configurations are modified to reflect wave  
294 effects on the atmosphere and the ocean. In the Mellor-Yamada-Nakanishi-Niino planetary  
295 boundary layer scheme (MYNN; Nakanishi and Nino, 2009), the surface roughness,  $z_0$ , is  
296 modified to include the effect of waves based on the following formulation,

删除了: domain includes

删除了: with a

删除了: for all model components

删除了: lead

321

$$z_0 = 1200H_s \left( \frac{H_s}{L_{wave}} \right)^{4.5} + \frac{0.11\nu}{u_*} \quad (22)$$

301

302

303

304

305

306

307

308

309

310

311

312

313

314

315

316

317

318

319

320

where  $\nu$  is the viscosity, and  $u_*$  is the friction velocity (Taylor and Yelland, 2001; Warner et al., 2010). For the interaction of ocean waves and currents, the vortex-force (VF) formulation is applied that represents conservative (e.g., vortex and Stokes-Coriolis forces) and non-conservative wave effects. The non-conservative wave effects in the VF formulation include wave accelerations for currents and wave-enhanced vertical mixing (Kumar et al., 2012; Uchiyama et al., 2010). The dissipated wave energy due to surface wave breaking and whitecapping is transferred to the ocean surface layer as additional turbulent kinetic energy, which in turn enhances the vertical mixing. For the effect of currents on the dispersion relation in wave propagation, we employ a depth-weighted current to account for the vertically-sheared flow following Kirby and Chen (1989). As discussed in previous studies (e.g., Naughten et al., 2017; Yang et al., 2022), the upwind third-order advection (U3H, Table 1) scheme, which is an oscillatory scheme, can lead to increased non-physical frazil ice formation. To address this issue, we implement the upwind flux limiter suggested by Leonard and Mokhtari (1990) to reduce false extrema caused by the oscillatory behavior of the U3H scheme. The value of yielding strain  $\epsilon_c$ , described in Section 2.3 is chosen as  $\cong 3 \times 10^{-5}$  (Dumont et al., 2011; Horvat and Tzipermann, 2015; Langhorne et al., 1998). The floe welding parameter in the thermodynamic term  $\mathcal{L}_T$ , is chosen as  $1 \times 10^{-7} \text{ km}^{-2}\text{s}^{-1}$ . Roach et al. (2018b) found a lower bound of floe welding parameter as  $1 \times 10^{-9} \text{ km}^{-2}\text{s}^{-1}$  in the autumn Arctic based on the observations. Also, the floe welding process only occurs in the freezing condition (Roach et al.,

2018a), and the freezing condition is determined by net ice mass increase by thermal mass

删除了: For the user-defined coefficients in the

323 change (see Figure 3). The floe welding parameter will behave like a step function during the  
324 freeze-thaw transition. For the user-defined coefficients in equation (4), all experiments use the  
325 equally-redistributed formulation described in Section 2.3 with  $c_w$  as 0.8 and  $\alpha$  as 1.0. Based  
326 on the formation of  $\mathcal{L}_T$  in the equation (9) (see Roach et al., 2018a), the floe size change  
327 through the lateral surface is determined by both the floe size and the lateral melting rate. In  
328 the existing sea ice models, the lateral melting rate  $w_{lat}$  is all based on the empirical  
329 formulation suggested by Perovich (1983, hereafter P83),

$$w_{lat} = m_1 \Delta T^{m_2} \quad (23)$$

330 where  $\Delta T$  is the temperature difference between sea surface temperature (SST) and the freezing  
331 point, and  $m_1, m_2$  are empirical coefficients based on the observations from a single sea ice  
332 lead in the Canadian Arctic. This empirical formulation is also the default lateral melting rate  
333 in the CICE model. Maykut and Perovich (1987, hereafter MP87) showed a different approach  
334 to parameterize the lateral melting rate that includes the friction velocity  $u_*$  based on the  
335 observations from the Marginal Ice Zone Experiment, which is defined as,

$$w_{lat} = u_* m_3 \Delta T^{m_4} \quad (24)$$

337 Both formulations (Equ. 23, 24) are examined in this study (see Table 2). In the equation (2),  
338 the user-defined coefficients for the wave attenuation are set as  $c_2 = 1.06 \times 10^{-3}$  and  $c_4 =$   
339  $2.3 \times 10^{-2}$  (case 1), which follow the polynomial of Meylan et al. (2014, hereafter M14) from  
340 the observations with 10-25m floe in diameter in the Antarctic, and  $c_2 = 2.84 \times 10^{-4}$  and  
341  $c_4 = 1.53 \times 10^{-2}$  (case 2), which follow the polynomial of Rogers et al. (2018, hereafter R18)  
342 based on the observations for pancake and frazil ice in the Arctic.

---

344 In this study, a series of numerical experiments for the pan-Arctic sea ice simulation have  
345 been conducted, starting from January 1<sup>st</sup>, 2016 to December 31<sup>st</sup>, 2020. Table 2 provides the  
346 details of the configurations for these experiments, which allow us to examine the influence of  
347 ocean waves and related physical processes on Arctic sea ice simulation in the atmosphere-  
348 ocean-wave-sea ice coupled framework. Specifically, these experiments focus on 1) the  
349 comparison between constant FSD and prognostic FSD (Exp-CFSD and Exp-PFSD), 2) sea ice  
350 responses to different lateral melting rate parameterizations (Exp-CFSD, Exp-PFSD, Exp-  
351 LatMelt-C and Exp-LatMelt-P), 3) the difference between the equally-redistributed  
352 formulation and the Bretschneider formulation for floe fracturing (Exp-PFSD and Exp-  
353 WaveFrac-P), and 4) the contribution of different wave attenuation rates to sea ice changes  
354 (Exp-CFSD, Exp-PFSD, Exp-WaveAtt-C and Exp-WaveAtt-P).

## 355 4. Results

### 356 4.1 Constant vs. Prognostic floe size

357 Figure 2 shows the evolution of sea ice area (SIA) for all experiments conducted in this  
358 study (as well as the values of seasonal maximum and minimum SIA for all experiments are  
359 summarized in Table S1). SIA is calculated as the sum of the ice-covered area of all grid cells  
360 (cell-area times sea ice concentration). In addition to the evolution of SIA, the 2016-2020  
361 averaged March and September sea ice concentration (SIC) for all experiments are shown in  
362 Figure S1. Compared with Exp-CFSD, which uses a constant floe diameter (300m) in the  
363 lateral melting scheme (Steele, 1992), Exp-PFSD uses the equations described in Section 2.2  
364 to determine the prognostic FSD and related physical processes (see Table 2). With the



365 prognostic FSD, the evolution of SIA in Exp-PFSD (Fig. 2a, red line) shows smaller SIA in the  
366 melting months (June to September) and similar magnitude of SIA in other months compared  
367 to that of Exp-CFSD (Fig. 2a, blue line) during 2016-2018. After that, Exp-PFSD simulates  
368 smaller SIA than that of Exp-CFSD for most months during 2019-2020, especially for the  
369 seasonal maximum of 2019 and SIA after May 2020.

删除了: ,

370 Figure 3 shows the evolution of sea ice mass budget terms with cell-area weighted  
371 averaging over the entire model domain with a 15-day running-average for smoothing out high-  
372 frequency fluctuations for all experiments. The most notable difference between Exp-CFSD  
373 and Exp-PFSD is the magnitude of basal melt (red lines) and lateral melt (grey lines). In Exp-  
374 CFSD, basal melt plays the dominant role in reducing sea ice mass compared to lateral melt  
375 which has negligible contribution to the total mass change. As discussed in Maykut and  
376 Perovich (1987), the inclusion of friction velocity in calculating the lateral melting rate results  
377 in  $w_{lat} \rightarrow 0$  as  $u_* \rightarrow 0$ , which contributes to negligible lateral melt in Exp-CFSD. By contrast,  
378 Exp-PFSD with prognostic floe size shows that lateral melt has the major contribution in  
379 reducing ice mass (Fig. 3b), a result of smaller floe size near the ice edge simulated by Exp-  
380 PFSD (Fig. 10a). It is also notable that the increased lateral melt in Exp-PFSD tends to be  
381 compensated by the decreased basal melt (Fig. 3b). The overall ice melt due to oceanic  
382 processes in Exp-PFSD (i.e., the sum of lateral melt and basal melt) does not change  
383 significantly compared to that of Exp-CFSD (Fig. S2e). The melting potential in the CICE  
384 model of CAPS, the available energy from the ocean to melt sea ice, is defined as the vertical  
385 integral of the difference between ocean temperature and freezing point within the surface layer

删除了: that

删除了: .

---

389 [\(to 5-meter depth in CAPS\) from the ROMS model](#). When the available oceanic energy is less  
390 than the sum of heat fluxes used for lateral and basal melt, the CICE model performs a linear  
391 scaling to maintain the relative magnitude of heat fluxes for lateral and basal melt. Thus, the  
392 increased energy consumption by lateral melt due to smaller floe size reduces the available  
393 energy for basal melt. Such change between lateral and basal melt has been shown in some  
394 studies (e.g., Bateson et al., 2020, 2022; Roach et al., 2018a, 2019; Smith et al., 2022; Tsamados  
395 et al., 2015). Although the rough compensation, Exp-PFSD simulates more ice melted by the  
396 oceanic energy compared to Exp-CFSD from January to July (Fig. S2e).

397 Figure 4 shows the evolution of ice-ocean heat flux, the friction velocity at the ice-ocean  
398 interface, and the temperature difference between SST and freezing point for Exp-CFSD and  
399 Exp-PFSD. These variables are the average of ice-covered cells with at least 1% ice  
400 concentration, and the ice-ocean heat flux is weighted by the ice concentration so that the  
401 weighted heat flux represents the mean value of [the](#) cell, rather than the mean value of [the](#) ice-  
402 ocean interface. It should be noted that cells with negative values of the temperature difference  
403 (i.e., supercooled water) are forced to be zero. This is consistent with the treatment in the CICE  
404 model for the calculation of ice-ocean heat flux. As shown in Fig. 4a and Fig. S2e, the evolution  
405 of ocean-induced ice melt is consistent with that of the ice-ocean heat flux for both Exp-CFSD  
406 and Exp-PFSD. Both Exp-CFSD and Exp-PFSD show relatively similar evolution of the  
407 friction velocity (Fig. 4b). The temperature difference of Exp-PFSD is much smaller than that  
408 of Exp-CFSD (Fig. 4c). The ice-ocean heat flux is the total heat flux from ocean to ice through  
409 ice bottom surface and lateral surface. Although Exp-PFSD has smaller temperature difference

410 as well as the melting potential under ice-covered cells, the larger total ice surface area due to  
411 smaller floe size increases the efficiency of Exp-PFSD extracting energy from the ocean. The  
412 smaller temperature difference of Exp-PFSD and the compensation between lateral and basal  
413 melt suggest that the ocean surface layer of Exp-PFSD is closer to the freezing point compared  
414 to that of Exp-CFSD. Energy loss from the ocean through air-sea heat flux that further cools  
415 the upper ocean, freshwater input (e.g., ice melting, precipitation) that raises the freezing point,  
416 as well as non-physical numerical oscillations (Naughten et al., 2017; Yang et al., 2022), can  
417 lead to increased frazil ice formation of Exp-PFSD as shown in Fig. 3a-b and Fig. S2g.

删除了: more closed

删除了: oscillation

删除了: 2018

删除了: )

418 Figure 5 shows the heat flux budget at the ice surface averaged for all ice-covered cells.  
419 The positive ice-atmosphere heat fluxes of Exp-CFSD and Exp-PFSD in July (Fig. S3a)  
420 correspond to top melt in Fig. 3a-b and Fig. S2b (as well as Table S2). The ice-atmosphere heat  
421 flux not only determines the magnitude of ice surface melt in summer but also the energy loss  
422 from the ice interior in winter, which is crucial for ice growth. As shown in Fig. S3a, Exp-  
423 PFSD loses more energy to the atmosphere than that of Exp-CFSD in most winters. The  
424 conductive heat flux also shows similar evolution, suggesting that more energy is conducted to  
425 the ice top from ice layers below in Exp-PFSD (Fig. S3b). The loss of ice energy then  
426 contributes to increased ice growth at the ice bottom as shown in Fig. 3a-b and Fig. S2f (as  
427 well as Table S2). Generally, the net shortwave flux of Exp-PFSD is larger (ice gains more  
428 energy) than that of Exp-CFSD, especially during the melting season (Fig. S3c). In contrast to  
429 the net shortwave flux, for most of the time, the net longwave flux of Exp-PFSD is smaller (i.e.,  
430 ice loses more energy) than that of Exp-CFSD (Fig. S3d). Exp-PFSD loses more energy

删除了: the

436 through sensible heat flux compared to Exp-CFSD (Fig. S3e). For latent heat flux, there ~~are~~ no  
437 common features between Exp-PFSD and Exp-CFSD, suggesting the difference in the  
438 simulation of atmospheric transient systems (Fig. S3f).

439 The ice mass budget in Fig. 3 is not directly related to the evolution of ~~SIA~~ in Fig. 2 since  
440 each process acts differently in changing ~~SIA~~. For vertical processes (i.e., top melt, basal melt),  
441 ice must be vertically-melted completely to reduce ~~SIA~~. Lateral melt, on the contrary, can  
442 directly reduce ~~SIA~~ (Smith et al., 2022). Figure 6 shows the evolution of ~~SIA~~ changes due to  
443 thermal processes (top melt, basal melt, lateral melt, frazil ice formation) and dynamical  
444 processes (transport, ridging). For thermal area changes, Exp-PFSD (red line), in general,  
445 shows comparable ice area changes ~~compared to Exp-CFSD (blue line)~~ for most of the period  
446 (Fig. 6a). Compared with Fig. S2g, the timings that Exp-PFSD shows more thermally-increased  
447 ice area correspond to increased frazil ice formation, which primarily occurs in open water. In  
448 contrast to thermal area changes, dynamical area changes of Exp-PFSD ~~tend~~ to reduce ice area  
449 relative to that of Exp-CFSD (Fig. 6e). Dynamically-induced area changes are partly due to the  
450 ridging scheme (Lipscomb et al., 2007) that favors the conversion of thin ice to thicker ice and  
451 reduces total ice area but preserves the total volume. In general, Exp-PFSD has ~~a~~ higher fraction  
452 of ice in the thinner ITD range than Exp-CFSD.

453 Based on geographic features, we define the following subregions for further analysis: 1)  
454 Barents and Greenland Seas (ATL, 45W-60E, 65N-85N), 2) Laptev and Kara Seas (LK, 60E-  
455 150E, 65N-85N), and 3) Beaufort, Chukchi, and East Siberian Seas (BCE, 150E-120W, 65N-  
456 85N, see black boxes in Fig. 1 for the geographic coverage of subregions). The ~~fetches~~ of ATL,

删除了: is

删除了: sea ice area

删除了: ice area

删除了: ice area

删除了: ice area

删除了: sea ice area

删除了: to increased ice area

删除了: tends

删除了: fetch

466 LK<sub>2</sub> and BCE regions are limited by the surrounding continents and the seasonal evolution of  
467 ice-covered areas. The ATL region is only partially-limited by ice-covered areas while the LK  
468 and BCE regions can be fully-covered by sea ice in winter. Figure 7 shows the evolution of sea  
469 ice extent, sea ice area, domain-averaged significant wave height, melting potential, and heat  
470 flux at the ocean surface (FLUX<sub>OCN</sub>, including ice-ocean and atmosphere-ocean interfaces) of  
471 Exp-CFSD and Exp-PFSD. As shown in Fig. 7a-i, it is clear that the higher (lower) significant  
472 wave height corresponds to less (more) regional ice coverage for all subregions. For the melting  
473 potential (Fig. 7j-l), the difference between Exp-CFSD (blue line) and Exp-PFSD (red line) in  
474 August, in general, is correlated with FLUX<sub>OCN</sub> in July (Fig. 7m-o). The more (less) incoming  
475 heat flux to the ocean due to less (more) ice-covered area increases (decreases) energy stored  
476 in the ocean surface layer. However, FLUX<sub>OCN</sub> alone cannot explain the difference in the  
477 melting potential for the entire period. For example, Exp-PFSD shows more melting potential  
478 after December,2019 in the ATL region (Fig. 7i), and more melting potential in December,2017  
479 in the LK region (Fig. 7k) compared to Exp-CFSD. These timings do not show corresponding  
480 FLUX<sub>OCN</sub> in the preceding month, suggesting the contribution of different processes. Figure 8  
481 shows the evolution of wave energy dissipation due to whitecapping and the difference of  
482 temperature profile in the upper 150m for Exp-CFSD and Exp-PFSD. As described in section  
483 3, wave energy dissipation increases the turbulent kinetic energy in the surface layer and thus  
484 vertical mixing. Dissipation due to surface wave breaking is zero for most of the period.  
485 Occasionally, there are non-zero dissipations due to surface wave breaking for Exp-CFSD and  
486 Exp-PFSD. The evolution of wave dissipation due to whitecapping (Fig. 8a-c) is in good

删除了: area

删除了: area

删除了: winters

删除了: c

删除了: 7d

删除了: 7e

删除了: of

删除了: ,

删除了: d<sub>1</sub>

删除了: ,

删除了: d<sub>2</sub>

删除了: corresponded

删除了: at

500 agreement with that of significant wave height in Fig. [7g-i](#). This suggests that stronger wave  
501 conditions associated with less ice-covered [areas](#) increase the effect of vertical mixing.  
502 Combined with the warmer upper ocean in Exp-PFSD after January, 2020 in [the](#) ATL region  
503 and in December, 2017 in [the](#) LK region in Fig. 8d-e, the strengthened vertical mixing brings  
504 warmer water of the subsurface upward and maintains/increases the melting potential in the  
505 subregions. [Figure 8d-f also shows that the warmer signal in the upper ocean \(at least to 60m](#)  
506 [depth\) of Exp-PFSD persists after July 2018 in the ATL region while the LK and BCE regions](#)  
507 [show seasonal oscillation of ocean temperature in the upper ocean for the entire simulation.](#)  
508 [Combined with the regional SIA shown in Figure 7d-f, seasonal fully ice-covered states in the](#)  
509 [LK and BCE regions force the upper ocean to restore to certain states \(i.e., near freezing point](#)  
510 [under sea ice, near zero melting potential shown in Fig. 7k-l\) for both Exp-CFSD and Exp-](#)  
511 [PFSD, which might mitigate the effects of ocean wave activities and other processes on the](#)  
512 [upper ocean. With less restoring effect by sea ice on the upper ocean in the ATL region, the](#)  
513 [difference of thermally-induced mass change between Exp-PFSD and Exp-CFSD shows a](#)  
514 [larger variation once the upper ocean difference starts to persist after July 2018 \(Fig. 8d, S4d\)](#)  
515 [while the variations in the LK and BCE regions remain relatively unchanged for the entire](#)  
516 [simulation \(Fig. S4e-f\).](#)

517 Additionally, atmospheric circulation responds to the changes in [the](#) spatial distribution of  
518 sea ice (Fig. S1). As shown in Figure [S5](#), Exp-PFSD tends to have anomalous anti-cyclonic  
519 circulations in September compared to Exp-CFSD, but there is no consistent center of [action](#)  
520 during the entire period. In March, Exp-PFSD tends to simulate anomalous cyclonic

删除了: 7c

删除了: area

删除了: ,

删除了: ,

删除了: S4

删除了: actions

527 circulations in the Barents-Kara Sea for most of the years compared to Exp-CFSD, except in  
528 2019. The responses in the atmospheric state in both experiments also influence sea ice  
529 movement, which further contributes to the regional ice differences in Fig. 7a-f, as well as the  
530 heat flux budgets in Fig. S3.

删除了: response

删除了: b

#### 531 4.2 Sensitivity to lateral melting rate parameterization

532 In addition to the floe size as discussed in the above section, the lateral melting rate ( $w_{lat}$ )  
533 is an important factor contributing to the relative strength of lateral and basal melt. As described  
534 in section 3, we conduct the experiments with the lateral melting rate suggested by Perovich  
535 (1983, P83), and Maykut and Perovich (1987, MP87) (see Table 2), to examine the sensitivity  
536 of Arctic sea ice simulation to different lateral melting rate parameterizations. As shown in Fig.  
537 2b, the simulated summer sea ice area of Exp-LatMelt-C (green line) and Exp-LatMelt-P (grey  
538 line), in general, is larger than those of Exp-CFSD (blue line) and Exp-PFSD (red line).

539 As shown in the sea ice mass budget (Fig. 3a, 3c), Exp-LatMelt-C, which does not include  
540 the friction velocity in the formulation (Equ. 23), but keeps other model configurations same  
541 as Exp-CFSD only shows a slightly larger contribution to lateral melt during summer months  
542 (Fig. S6d). Also, the contribution to basal melt by Exp-LatMelt-C is generally smaller than that  
543 in Exp-CFSD (Fig. S6c). Similar to the experiments with the MP87 scheme, Exp-LatMelt-P  
544 with the prognostic FSD also shows the compensation between lateral melt and basal melt  
545 compared to Exp-LatMelt-C (Fig. 3c, 3d). Exp-LatMelt-P shows stronger lateral melt  
546 compared to Exp-PFSD, which is contributed by the P83 formulation (Fig. S6d). Despite the  
547 stronger lateral melt in Exp-LatMelt-P, its basal melt is smaller compared to Exp-PFSD (Fig.

删除了: show

删除了: S5d

删除了: S5c

删除了: show

删除了: S5d

555 [S6c](#)). Thus, the ocean-induced melt of Exp-LatMelt-P is broadly similar to that of Exp-PFSD.

删除了: S5c

556 The result of Exp-LatMelt-P and Exp-PFSD suggests that the changes [in](#) lateral and basal melt

删除了: of

557 due to different lateral melting rate parameterizations are mostly controlled by the available

558 energy from the ocean (i.e., melting potential).

559 Exp-LatMelt-P simulates more basal growth in winter (Fig. [S6f](#)), which is contributed by

删除了: S5f

560 more energy loss to the atmosphere (Fig. 5a), in comparison to Exp-PFSD. Also, more frazil

561 ice formation is simulated in Exp-LatMelt-P than Exp-PFSD during most of [the](#) simulation

562 period (Fig. [S6g](#)). The combined effects of [the](#) above processes lead to [Exp-LatMelt-P](#) [showing](#)

删除了: S5g

删除了: that

删除了: shows

563 less total ice melt in summer and similar ice growth in winter compared to Exp-PFSD (Fig.

删除了: S5a

564 [S6a](#)). Due to more frazil ice formation, Exp-LatMelt-P shows more thermally-increased ice

565 area compared to Exp-PFSD (Fig. 6, Fig. [S6g](#)). Frazil ice formation reduces open-water areas

删除了: S5g

566 and blocks the energy exchange between the atmosphere and the ocean. That is, the upper ocean

567 under sea ice in Exp-LatMelt-P receives less incoming flux from the atmosphere (i.e., solar

568 radiation) during April to September (not shown) to balance the energy consumption by ice

569 melt, which leads to smaller ocean temperature difference compared to Exp-PFSD (Fig. 4c,

570 green and red lines).

571 Figure 9 shows the spatial distribution of sea ice concentration, sea surface temperature,

572 and friction velocity in September, [2020](#) for the experiments using MP87 and P83 schemes.

删除了: ,

573 Exp-CFSD, Exp-PFSD, and Exp-LatMelt-C simulate large areas with ice concentration less

574 than 5% (they are mostly much less than 1%, Fig. [9a-c](#)). In opposite to these three experiments,

删除了: 9a1-3

575 Exp-LatMelt-P does not show wide areas with non-zero and infinitesimal ice concentration



586 (Fig. 9d). Although these areas only account for a tiny fraction of total sea ice, they may still  
587 be a source of uncertainty for sea ice simulations. Ice-existed cells can be influenced by all  
588 processes involved in sea ice mass budget (Fig. 3) while ice-free cells can only be affected by  
589 frazil ice formation and dynamical advection. Under these small-ice areas, SST is well above  
590 the freezing point (Fig. 9e-h) and the friction velocity is mostly less than  $5 \times 10^{-4}$  m/s (Fig.  
591 9i-l). In our configuration of the CICE model, the minimum value of friction velocity is set to  
592  $5 \times 10^{-4}$  m/s. This suggests that the friction velocity is the limit factor for heat flux  
593 transferred into sea ice in the small-ice areas. For basal heat flux, the formulation in the CICE  
594 model is based on Maykut and McPhee (1995), which is controlled by the friction velocity and  
595 the temperature difference. Thus, basal heat fluxes with small friction velocities may not be  
596 large enough to satisfy the energy convergence (in conjunction with conductive heat flux at the  
597 ice bottom) at the ice-ocean interface to melt ice if the temperature difference does not show a  
598 larger magnitude. Since the MP87 scheme includes the friction velocity, lateral heat flux is also  
599 limited in small-ice areas. Exp-PFSD has a much smaller floe size (compared to 300m) in these  
600 small-ice areas, but the increased strength of lateral melt does not overcome the limitation of  
601 friction velocity to melt ice completely (Fig. 9b). The P83 scheme, which does not include the  
602 friction velocity, is controlled by the temperature difference, but the effect of lateral melting in  
603 Exp-LatMelt-C is largely constrained by constant 300m floe diameter. Liang et al. (2019)  
604 suggested these small-ice areas can be eliminated by assimilating SST observations. The results  
605 of Exp-LatMelt-P suggest a model physics approach that considers the prognostic FSD and the  
606 lateral melting rate to reduce the coverage of small-ice near the ice-edge.

删除了: 9a4

删除了: 9b

删除了: 9c

删除了: lateral melting

删除了: 9a2

删除了: lateral melting

删除了: that

删除了: theses

---

### 615 4.3 Sensitivity to floe-fracturing parameterization

616 The equally-redistributed formulation (hereafter PF1) for floe-fracturing described in  
617 section 2.3.a does not have preferential floe size after fracturing (i.e., a stochastic process).  
618 However, the size of fractured floes can be predicted based on the properties of surface ocean  
619 waves, particularly wavelength (Dumont et al. 2011; Horvat and Tziperman, 2015). In this  
620 section, we conduct an experiment (Exp-WaveFrac-P, see Table 2), which utilizes a semi-  
621 empirical wave spectrum to redistribute fractured floes (see section 2.3.b for details and  
622 hereafter PF2) to explore the effects of different wave-fracturing formulations on Arctic sea ice  
623 simulation. As shown in Fig. 2c, Exp-WaveFrac-P (orange line) simulates larger SIA in summer  
624 and comparable SIA in winter compared to that of Exp-PFSD (red line).

625 By applying different formulations for floe-fracturing (as well as different lateral melting  
626 rate formulations), the FSD responds accordingly. To quantify the responses of FSD associated  
627 with different physical configurations (Table 2), the representative floe radius  $r_a$ , as well as its  
628 tendency due to different processes in the equation (9) are utilized and calculated as (Roach et  
629 al., 2018a),

$$630 \quad r_a = \frac{\int_{\mathcal{R}} \int_{\mathcal{H}} r f(r, h) dr dh}{\int_{\mathcal{R}} \int_{\mathcal{H}} f(r, h) dr dh} \quad (25)$$

$$631 \quad \frac{dr_a}{dt} = \frac{\int_{\mathcal{R}} \int_{\mathcal{H}} r \frac{df(r, h)}{dt} dr dh}{\int_{\mathcal{R}} \int_{\mathcal{H}} f(r, h) dr dh} \quad (26)$$

632 Figure 10 shows the spatial distribution of the representative floe radius in winter and  
633 summer for all experiments with the prognostic FSD. As described in section 3,  $L(r, h)$  is  
634 initialized by the power law distribution with the exponent as 2.1 for all experiments. Exp-

删除了: ice area

删除了: ice area

删除了: with respect

638 WaveFrac-P shows [a](#) smaller floe radius in the Chukchi and East Siberian Seas and north of  
639 Greenland at the early stage of simulation compared to experiments using PF1 formulation (Fig.  
640 [10a-o](#), upper panel). Small-floe areas in Exp-WaveFrac-P are mostly contributed by the effect  
641 of wave-fracturing where decreasing tendency of floe radius can extend further into the central  
642 Arctic from the Atlantic and the Bering Strait compared to PF1 experiments (Fig. [S7](#)). After  
643 September, 2016, the representative floe radii of PF experiments emerge, that is, Exp-  
644 WaveFrac-P has [a](#) smaller floe size compared to PF1 experiments for both winter and summer  
645 (Fig. 10a-[p](#)). In summer, Exp-WaveFrac-P shows mostly fully-fractured floe (<10m, Fig. [10k-](#)  
646 [o](#), bottom panel). The stronger wave-fracturing shown in Exp-WaveFrac-P is partly contributed  
647 by the semi-empirical wave spectrum used in PF2. The simulated wave parameters under ice-  
648 covered area are mostly with  $H_s < 0.01$  m/s and  $T_p > 15$  s. The constructed wave spectrum  
649 and amplitude based on simulated wave parameters under sea ice and equations (17) and (18)  
650 still include the contribution from high-frequency waves ( $T = 2s$  bin), especially in the ice  
651 pack far from the ice edge. The high-frequency waves only account for [a](#) small fraction in the  
652 wave period distribution  $\bar{P}(T)$ , and have small wave amplitude  $A(T)$  ( $\sim 7 \times 10^{-4}m$ ). The  
653 strain of [the](#) high-frequency bin based on equation (20) still exceeds the yielding strain and  
654 then fractures [ice](#) floe into the smallest floe size category. Observational and numerical studies  
655 showed that high-frequency waves rapidly decay and reach [the](#) “zero” transmission state for  
656 high-frequency waves when traveling under sea ice (e.g., Collins et al., 2015; Liu et al., 2020).  
657 Despite the over-fracturing behavior shown in Exp-WaveFrac-P, the prevalence of small-floe  
658 does not translate into the stronger ocean-induced ice melt but weaker melt in summer

删除了: 10a1-c1

删除了: S6

删除了: ,

删除了: c

删除了: 10c

664 compared to Exp-PFSD (Fig. 3d-e, Fig. [S8e](#)), indicating the limiting role of melting potential.  
665 The weaker ocean-induced ice melt in [the](#) summer of Exp-WaveFrac-P [corresponds](#) to smaller  
666 ice-ocean heat fluxes (Fig. [S9a](#)), which is contributed by both smaller friction velocity and  
667 temperature difference (Fig. [S9b-c](#)).

删除了: S7e

删除了: is corresponded

删除了: S8a

删除了: S8b

#### 668 4.4 Sensitivity to wave-attenuation parameterization

669 We have shown that ocean waves can alter the upper ocean through wave-enhanced  
670 mixing, which may affect sea ice locally (Fig. 8, see section 4.1). The results from PF1 and  
671 PF2 experiments imply that the simulated wave parameters can determine how ice floes are  
672 fractured. As described in section 2.1, we can choose different coefficients in equation (2) to  
673 control the wave attenuation rate of each frequency. In this section, we conduct experiments  
674 using R18 coefficients (see section 3 and Table 2) to study the impacts of wave-attenuation rate  
675 on Arctic sea ice simulation. The simulated sea ice area in Exp-WaveAtt-C (Fig. 2d, light-blue  
676 line) resembles that in Exp-CFSD (Fig. 2d, blue line) before 2019. After 2019, Exp-WaveAtt-

677 C simulates smaller [SIA](#) compared to Exp-CFSD. Since both Exp-CFSD and Exp-WaveAtt-C  
678 use constant floe size, which allows us to neglect the effect of [the](#) spatial distribution of floe  
679 size and [the](#) MP87 [scheme](#), which [makes](#) lateral melt have a negligible contribution (Fig. [S10d](#)),  
680 basal melt is the primary factor for the ocean-induced ice melt during the entire period (Fig. 3a,  
681 3f, and Fig. [S10e](#)). The strength of basal melt in Exp-WaveAtt-C is weaker than that in Exp-  
682 CFSD from April, 2018 to January, 2020 (Fig. [S10c](#)). Basal growth of Exp-WaveAtt-C is also  
683 smaller than that of Exp-CFSD in the winter of 2018 and 2019 (Fig. [S10f](#)). Compared to Exp-  
684 CFSD, Exp-WaveAtt-C shows stronger top melt in [the](#) summer of 2018 (Fig. [S10b](#)). The

删除了: ice area

删除了: lateral melting rate

删除了: make

删除了: S9d

删除了: S9e

删除了: ,

删除了: ,

删除了: S9c

删除了: S9f

删除了: S9b

699 combined effects of the above processes lead to a thinner ice state in Exp-WaveAtt-C before  
700 2019 (Fig. S10a). The thinner state of Exp-WaveAtt-C in the winter of 2019 causes more open  
701 water be created by basal melt (regardless of its smaller magnitude) and thus smaller SIA (Fig.  
702 2d), which is also shown in the thermally-induced ice area changes that Exp-WaveAtt-C has  
703 smaller magnitude in the corresponded period (Fig. 6d). As discussed in section 4.1, top melt  
704 and basal growth is in good agreement with the ice-atmosphere heat flux (Fig. S10, S11a). That  
705 is, ice mass and area changes described above are mainly driven by the ice-atmosphere heat  
706 flux associated with the atmospheric responses to the changes in ocean wave conditions.

707 Different from the M14 experiments, the simulated SIA of Exp-WaveAtt-C (light-blue  
708 line) and Exp-WaveAtt-P (yellow line) show relatively similar evolution during 2016-2020  
709 (Fig. 2d). The R18 coefficients represent weaker wave attenuation relative to the M14  
710 coefficients. Thus, ocean waves in the R18 experiments are expected to transmit further into  
711 the ice pack while maintaining relatively higher wave energy. To quantify to what extent the  
712 ice can be affected by ocean waves, we calculate the wave-affected extent (WAE), which is  
713 defined as the sum of the area of cells with ice concentration greater than 15% and significant  
714 wave height greater than 30cm (Cooper et al., 2022). Figure 11 shows the evolution of WAE  
715 for the M14 and R18 experiments with a 15-day running average to smooth the high-frequency  
716 changes of wave conditions. The weaker attenuation in Exp-WaveAtt-C and Exp-WaveAtt-P  
717 results in generally larger WAE compared to Exp-CFSD and Exp-PFSD (as well as all previous  
718 experiments with M14 coefficients, not shown). The direct impact of larger WAE in Exp-  
719 WaveAtt-P is that the representative floe radius is mostly smaller than 10m (fully-fractured by

删除了: S9a

删除了: make

删除了: -

删除了: S9, S10a

删除了: sea ice area

删除了: wave

726 ocean waves) (Fig. 10p-t). The decreasing tendency of floe radius due to wave-fracturing is the  
727 dominant factor contributing to the fully-fractured condition (Fig. S7). Similar to Exp-  
728 WaveFrac-P, the fully-fractured condition does not lead to stronger ocean-induced melt due to  
729 limited oceanic energy (Fig. 3b, 3e, 3g, S10e).

删除了: 10d

删除了: contributed

删除了: S6

删除了: S9e

## 730 5. Conclusions and Discussions

731 This study investigates the impacts of ocean waves on Arctic sea ice simulation based on  
732 a newly-developed atmosphere-ocean-wave-sea ice coupled model, which is built on the  
733 Coupled Arctic Prediction System (CAPS) by coupling the Simulating Waves Nearshore  
734 (SWAN) and the implementation of the modified joint floe size and thickness distribution  
735 (FSTD). A set of pan-Arctic experiments with different configurations of FSD-related  
736 processes are performed for the period 2016-2020. Specifically, we examine the contrasting  
737 behaviors of sea ice between constant and prognostic floe size, the responses of sea ice to  
738 different lateral melting rate formulations, and the sensitivity of sea ice to the simulated wave  
739 parameters under the atmosphere-ocean-wave-sea ice coupled framework.

740 The results of FSD-fixed and FSD-varied experiments show that the simulated sea ice  
741 area is generally lower with smaller floe size associated with physical processes that change  
742 FSD. According to sea ice mass budget analysis, smaller floe size contributes to increased  
743 lateral melt, but its effect is reduced by decreased basal melt. The combined effects of lateral  
744 and basal melt associated with smaller floe size result in relatively more ice melt by the ocean  
745 energy, which is similar to previous studies (e.g., Bateson et al., 2022; Roach et al., 2019; Smith  
746 et al., 2022). The simulations in Smith et al. (2022) with varying lateral melting strength based

---

751 on the Community Earth System Model version 2 (CESM2) with a slab-ocean model showed  
752 minimal change in frazil ice formation. In our simulation with a full ocean model, the enhanced  
753 ice melt by the ocean, though it is partially balanced by increased frazil ice formation due to  
754 the depletion of melting potential in the surface layer. This suggests negative feedback from  
755 the full ocean physics. Our simulations also show that the prevalence of small floes does not  
756 necessarily lead to stronger ice melting due to limited oceanic energy. To further illustrate the  
757 constraint role of limited oceanic energy, the mixed layer depths (MLDs) based on 0.1 degree  
758 Celsius difference relative to the surface temperature (e.g., Courtois et al., 2017, their Table 2)  
759 for Exp-CFSD and Exp-PFSD are shown in Figure 12. In general, Exp-CFSD and Exp-PFSD  
760 (as well as other experiments, not shown) exhibit similar evolution of MLD, that is MLD is  
761 deeper (up to 150m) in March and shallower (up to 80m) in September. MLD in the open  
762 waters is broadly similar across all experiments and MLD near the ice edge (15% ice  
763 concentration, black contour in Fig. 12) is shallower (10-30m) relative to other areas. In March,  
764 MLDs under ice-covered areas become deeper as lead time increases. To calculate the heat  
765 content within MLD, the same approach for calculating melting potential in the ROMS model  
766 is used, which is defined as the vertical integral from the surface to MLD of the difference  
767 between ocean temperature and freezing point. The calculated values of heat content and  
768 melting potential have the same unit ( $W/m^2$ ) and directionality (positive downward) as ice-  
769 ocean heat flux, and they represent the “maximum” heat flux that the ice can extract. Figures  
770 13 and 14 show the heat content of MLD and melting potential for Exp-CFSD and Exp-PFSD  
771 in March and September. As shown in Fig. 13-14, Exp-PFSD shows less melting potential (0-

772 5m) and the heat content within MLD under ice-covered areas compared to Exp-CFSD. This  
773 feature is more pronounced in September than in March. Also, heat content in MLD near the  
774 ice edge of Exp-PFSD reduces more than other ice-covered areas compared to that of Exp-  
775 CFSD, suggesting the role of ice-ocean heat flux. Figures 13 and 14 further support the  
776 constraint role of limited oceanic energy to ice melting with respect to varied floe size not only  
777 in the surface layer (i.e., melting potential) but also in the mixed layer.

778 Our fully-coupled simulations also show that atmospheric states respond to changing ice  
779 distributions and then modify the energy budget at the ice surface that determines top melt in  
780 summer and basal growth in winter. The FSD-varied experiments, in general, show more  
781 energy loss from ice to the atmosphere in winter, and all experiments show year-to-year  
782 variations of energy gain for sea ice in summer.

783 The depletion of ocean energy in the surface layer as well as enhanced frazil ice formation  
784 are the direct responses to the changes of ice-ocean coupling with the prognostic FSD. The  
785 fractured sea ice enlarges the ice-ocean heat flux while the freezing temperature is still  
786 determined by the sea surface salinity in the ocean model. However, the local salinity at the  
787 ice-ocean interface can be significantly lower than sea surface salinity, and thus higher freezing  
788 temperature locally due to the meltwater from sea ice (e.g., the false-bottom, Notz et al., 2003).  
789 Schmidt et al. (2004) proposed the ice-ocean heat flux formulation that considers the local  
790 salinity equilibrium but its formulation is only for the ice-bottom interface. The generalization  
791 of ice-ocean heat flux with the consideration of local salinity equilibrium for both bottom and  
792 lateral interface might yield a more realistic ice-ocean coupled simulation. Although the lateral

删除了:



794 melting rate formulation does not have ~~a~~ major effect on the simulated floe size distribution,  
795 the simulated sea ice area and ice mass budget are sensitive to the choice of the formulation.  
796 The lateral melting rate formulations applied in this study as well as previous laboratory results  
797 are not related ~~to~~ the ice properties (i.e., ice thickness and floe size, Josberger and Martin, 1981;  
798 Maykut and Perovich, 1987; Perovich, 1983). A recent laboratory study suggested that the  
799 lateral melting rate is a function of temperature difference and the ratio of floe size to ice  
800 thickness (Li et al., 2021). Smith et al. (2022) also suggested that Arctic sea ice simulation can  
801 be sensitive to the lateral melting rate of Perovich (1983) with different weights on each ice  
802 thickness category. Further studies are required to investigate improved lateral melting rate  
803 parameterization with observational constraints (e.g., data from the MOSAiC campaign in  
804 2020, Nicolaus et al., 2021) within the prognostic FSD framework.

805 As discussed in Horvat and Tziperman (2015), the FTSD is sensitive to the wave  
806 attenuation coefficients. Our simulations also show substantially contrasting behaviors in the  
807 simulated floe size distribution associated with simulated wave parameters, suggesting that  
808 several aspects need further investigation. First, the empirical wave attenuation (i.e., IC4M2)  
809 may have reasonable performance in simulating the changes of wave energy spectrum locally  
810 with specific ice conditions (e.g., Liu et al., 2020). However, the dissipation of wave energy  
811 varies spatially for the pan-Arctic (as well as pan-Antarctic) scale simulation with the different  
812 sea ice properties (i.e., ice concentration, ice thickness, floe size). Thus, a viscous boundary  
813 layer model (Liu et al., 1991) or a viscoelastic model (Wang and Shen, 2010) for wave  
814 attenuation, which provides spatially-varied wave attenuation with respect to sea ice properties,

删除了: the

---

816 might be able to give more realistic simulations in the wave-fracturing process and thus the  
817 floe size distribution. Also, the current implementation of sea ice effects in the SWAN model  
818 does not include the reflection and scattering due to sea ice, which redistributes the wave energy  
819 spatially and potentially changes the wave-fracturing behavior. Second, the probability of floe-  
820 fracturing  $Q(r)$  in both formulations applied in this study are uncertain. Both formulations  
821 result in floe-fracturing into smaller floe size categories within a short time interval as long as  
822 the simulated wave parameters satisfy the yielding strain. This strong contribution in the wave-  
823 fracturing term is not easily balanced by the floe-welding term. The floe-welding term (Roach  
824 et al., 2018a, b) acts to reduce the floe number density so that it is less effective in increasing  
825 the representative floe radius if the floe is mostly fractured with the smallest floe size. Third,  
826 the attenuated wave energy by sea ice does not influence sea ice conditions in this study. As  
827 suggested by Longuet-Higgins and Steward (1962), the attenuated wave energy is transferred  
828 into the ocean (as we described in section 3 for wave-enhanced mixing) or sea ice. For sea ice,  
829 the transferred energy acts as a stress, called wave radiation stress (WRS), pushing sea ice to  
830 the direction of wave propagation. By including the WRS in the momentum equation of ice,  
831 the WRS then can affect sea ice drift (e.g., Boutin et al., 2020).

832 For quantitative applications (e.g., forecasting sea ice), more observations (especially  
833 ocean waves under sea ice and FSD) are needed to reduce uncertainties in the atmosphere-  
834 ocean-wave-sea ice coupled model, particularly wave-related processes in ice-covered regions.  
835 Horvat et al. (2019) developed a new technique to retrieve pan-Arctic scale FSD climatology  
836 and seasonal cycle from CryoSat-2 radar altimeter and this method can resolve floe size from

删除了: -

删除了: satisfying

删除了: particular

---

840 300 m to 100 km and potentially up to 20 m scale if applied to ICESat-2 data. ICESat-2  
841 altimetry also provides a new opportunity to observe ocean waves in sea ice at hemispheric-  
842 scale coverage by directly observing the vertical displacements of the ice surface (e.g., Horvat  
843 et al., 2020). In situ observations, despite their limited spatial coverage, are valuable wave  
844 spectra measurements for wave-physics validation and improvement (e.g., Cooper et al., 2022;  
845 Liu et al., 2020).  
846

删除了: applying

848 Code and data availability: The outputs of pan-Arctic simulations analyzed in this study  
849 are archived at <https://doi.org/10.5281/zenodo.7922725>.

删除了: simulation

删除了: in

850

851 Author contributions: CYY and JL designed the model experiments, developed the  
852 updated CAPS model, and wrote the manuscript, CYY conducted the experiments and analyzed  
853 the results. DC provided constructive feedback on the manuscript.

854

855 Competing interests: The authors declare that they have no conflict of interest.

856

857 Acknowledgements: This research is supported by the National Natural Science  
858 Foundation of China (42006188, 42376237), the National Key R&D Program of China  
859 (2018YFA0605901), and the Innovation Group Project of Southern Marine Science and  
860 Engineering Guangdong Laboratory (Zhuhai) (311021008).

861

---

864 **6. References**

- 865 Asplin, M. G., Scharien, R., Else, B., Howell, S., Barber, D. G., Papakyriakou, T., and  
866 Prinsenberg, S.: Implications of fractured Arctic perennial ice cover on thermodynamic  
867 and dynamic sea ice processes, *J. Geophys. Res. Oceans*, 119, 2327–2343,  
868 <https://doi.org/10.1002/2013JC009557>, 2014.
- 869 Bai, Q., and Bai, Y.: 7 - Hydrodynamics around Pipes, *Subsea Pipeline Design, Analysis, and*  
870 *Installation*, Gulf Professional Publishing, 153-170, [https://doi.org/10.1016/B978-0-12-](https://doi.org/10.1016/B978-0-12-386888-6.00007-9)  
871 [386888-6.00007-9](https://doi.org/10.1016/B978-0-12-386888-6.00007-9), 2014.
- 872 Bateson, A. W., Feltham, D. L., Schröder, D., Hosekova, L., Ridley, J. K., and Aksenov, Y.:  
873 Impact of sea ice floe size distribution on seasonal fragmentation and melt of Arctic sea  
874 ice, *The Cryosphere*, 14, 403–428, <https://doi.org/10.5194/tc-14-403-2020>, 2020.
- 875 Bateson, A. W., Feltham, D. L., Schröder, D., Wang, Y., Hwang, B., Ridley, J. K., and Aksenov,  
876 Y.: Sea ice floe size: its impact on pan-Arctic and local ice mass and required model  
877 complexity, *The Cryosphere*, 16, 2565–2593, <https://doi.org/10.5194/tc-16-2565-2022>,  
878 2022.
- 879 Battjes, J. A. and Janssen, J. P. F. M.: Energy loss and set-up due to breaking of random waves,  
880 *Proc. 16th Int. Conf. Coastal Engineering*, ASCE, 569-587,  
881 <https://doi.org/10.1061/9780872621909.034>, 1978.
- 882 Bennetts, L. G., O'Farrell, S., and Uotila, P.: Brief communication: Impacts of ocean-wave-  
883 induced breakup of Antarctic sea ice via thermodynamics in a stand-alone version of the  
884 CICE sea-ice model, *The Cryosphere*, 11, 1035–1040, [https://doi.org/10.5194/tc-11-1035-](https://doi.org/10.5194/tc-11-1035-2017)  
885 [2017](https://doi.org/10.5194/tc-11-1035-2017), 2017.
- 886 Bitz, C. M. and Lipscomb, W. H.: An energy-conserving thermodynamic sea ice model for  
887 climate study. *J. Geophys. Res.-Oceans*, 104, 15669–15677,  
888 <https://doi.org/10.1029/1999JC900100>, 1999.

---

889 Blanchard-Wrigglesworth, E., Donohoe, A., Roach, L. A., DuVivier, A., and Bitz, C. M.: High-  
890 frequency sea ice variability in observations and models. *Geophysical Research Letters*,  
891 48, e2020GL092356. <https://doi.org/10.1029/2020GL092356>, 2021.

892 Booij, N., Ris, R. C., and Holthuijsen, L. H.: A third-generation wave model for coastal regions.  
893 Part I: Model description and validation. *Journal of Geophysical Research* 104 (C4),  
894 7649–7666, <https://doi.org/10.1029/98JC02622>, 1999.

895 Boutin, G., Lique, C., Ardhuin, F., Rousset, C., Talandier, C., Accensi, M., and Girard-Ardhuin,  
896 F.: Towards a coupled model to investigate wave–sea ice interactions in the Arctic  
897 marginal ice zone, *The Cryosphere*, 14, 709–735, <https://doi.org/10.5194/tc-14-709-2020>,  
898 2020.

899 Bretschneider, C. L.: Wave variability and wave spectra for wind-generated gravity waves,  
900 1959.

901 Briegleb, B. P. and Light, B.: A Delta-Eddington multiple scattering parameterization for solar  
902 radiation in the sea ice component of the Community Climate System Model. (No.  
903 NCAR/TN-472+STR). University Corporation for Atmospheric Research,  
904 <https://doi.org/10.5065/D6B27S71>, 2007.

905 Casas-Prat, M., and Wang, X.: Sea ice retreat contributes to projected increases in extreme  
906 Arctic ocean surface waves. *Geophysical Research Letters*, 47, e2020GL088100.  
907 <https://doi.org/10.1029/2020GL088100>, 2020.

908 Cassano, J. J., Higgins, M. E., and Seefeldt, M. W.: Performance of the Weather Research and  
909 Forecasting Model for Month-Long Pan-Arctic Simulations. *Monthly Weather Review*,  
910 139, 11, 3469-3488, <https://doi.org/10.1175/MWR-D-10-05065.1>, 2011.

911 Cavalieri, D. J., Parkinson, C. L., Gloersen, P., and Zwally, H. J.: updated yearly. Sea Ice  
912 Concentrations from Nimbus-7 SMMR and DMSP SSM/I-SSMIS Passive Microwave  
913 Data, Version 1. Boulder, Colorado USA. NASA National Snow and Ice Data Center  
914 Distributed Active Archive Center. <https://doi.org/10.5067/8GQ8LZQVL0VL>, 1996.

---

915 Chen, F. and Dudhia, J.: Coupling an advanced land surface–hydrology model with the Penn  
916 State–NCAR MM5 modeling system. Part I: Model implementation and sensitivity. *Mon.*  
917 *Wea. Rev.*, 129, 569–585, [https://doi.org/10.1175/1520-](https://doi.org/10.1175/1520-0493(2001)129<0569:CAALSH>2.0.CO;2)  
918 [0493\(2001\)129<0569:CAALSH>2.0.CO;2](https://doi.org/10.1175/1520-0493(2001)129<0569:CAALSH>2.0.CO;2), 2001.

919 Cole, S. T., Toole, J. M., Lele, R., Timmermans, M.-L., Gallagher, S. G., Stanton, T. P., Shaw,  
920 W. J., Hwang, B., Maksym, T., Wilkinson, J. P., Ortiz, M., Graber, H., Rainville, L., Petty,  
921 A. A., Farrell, S. L., Richter-Menge, J. A., and Haas, C.: Ice and ocean velocity in the  
922 Arctic marginal ice zone: Ice roughness and momentum transfer, *Elementa: Science of the*  
923 *Anthropocene*, 5, 55, <https://doi.org/10.1525/elementa.241>, 2017.

924 Collins, C. O., III, Rogers, W. E., Marchenko, A., and Babanin, A. V.: In situ measurements of  
925 an energetic wave event in the Arctic marginal ice zone, *Geophys. Res. Lett.*, 42, 1863–  
926 1870, <https://doi.org/10.1002/2015GL063063>, 2015.

927 Collins, C. O., and Rogers, W. E.: A Source Term for Wave Attenuation by Sea ice in  
928 WAVEWATCH III: IC4, NRL Report NRL/MR/7320–17-9726, 25pp. Available from  
929 <https://www7320.nrlssc.navy.mil/pubs.php>, 2017.

930 Collins, W. D., Rasch, P. J., Boville, B. A., McCaa, J., Williamson, D. L., Kiehl, J. T., Briegleb,  
931 B. P., Bitz, C., Lin, S.-J., Zhang, M., and Dai, Y.: Description of the NCAR Community  
932 Atmosphere Model (CAM 3.0). (No. NCAR/TN-464+STR). University Corporation for  
933 Atmospheric Research. <https://doi.org/10.5065/D63N21CH>, 2004.

934 Cooper, V. T., Roach, L. A., Thomson, J., Brenner, S. D., Smith, M. M., Meylan, M. H., and  
935 Bitz, C.M.: Wind waves in sea ice of the western Arctic and a global coupled wave-ice  
936 model. *Phil. Trans. R. Soc. A.*, 380, 20210258, <https://doi.org/10.1098/rsta.2021.0258>,  
937 2022.

938 [Courtois, P., Hu, X., Pennelly, C., Spence, P., and Myers, P. G.: Mixed layer depth calculation](https://doi.org/10.1016/j.ocemod.2017.10.007)  
939 [in deep convection regions in ocean numerical models, \*Ocean Modelling\*, 120, 67-78,](https://doi.org/10.1016/j.ocemod.2017.10.007)  
940 [http://dx.doi.org/10.1016/j.ocemod.2017.10.007](https://doi.org/10.1016/j.ocemod.2017.10.007), 2017.

---

941 Curry, J. A., Schramm, J. L., and Ebert, E. E.: Sea ice-albedo climate feedback mechanism, *J.*  
942 *Climate*, 8, 240–247, [https://doi.org/10.1175/1520-](https://doi.org/10.1175/1520-0442(1995)008<0240:SIACFM>2.0.CO;2)  
943 [0442\(1995\)008<0240:SIACFM>2.0.CO;2](https://doi.org/10.1175/1520-0442(1995)008<0240:SIACFM>2.0.CO;2), 1995.

944 Dobrynin, M., Murawsky, J., and Yang, S.: Evolution of the global wind wave climate in  
945 CMIP5 experiments, *Geophys. Res. Lett.*, 39, L18606,  
946 <https://doi.org/10.1029/2012GL052843>, 2012.

947 Dumont, D., Kohout, A., and Bertino, L.: A wave-based model for the marginal ice zone  
948 including a floe breaking parameterization, *J. Geophys. Res.*, 116, C04001,  
949 <https://doi.org/10.1029/2010JC006682>, 2011.

950 Freitas, S. R., Grell, G. A., Molod, A., Thompson, M. A., Putman, W. M., Santos e Silva, C. M.  
951 and Souza, E. P.: Assessing the Grell–Freitas convection parameterization in the NASA  
952 GEOS modeling system. *J. Adv. Model. Earth Syst.*, 10, 1266–1289,  
953 <https://doi.org/10.1029/2017MS001251>, 2018.

954 Gupta, M., and Thompson, A. F.: Regimes of sea-ice floe melt: Ice-ocean coupling at the  
955 submesoscales. *Journal of Geophysical Research: Oceans*, 127, e2022JC018894.  
956 <https://doi.org/10.1029/2022JC018894>, 2022.

957 Hasselmann, S., Hasselmann, K., Allender, J. H., and Barnett, T. P.: Computations and  
958 parameterizations of the nonlinear energy transfer in a gravity wave spectrum. Part II:  
959 Parameterizations of the nonlinear transfer for application in wave models, *J. Phys.*  
960 *Oceanogr.*, 15, 11, 1378–1391, [https://doi.org/10.1175/1520-](https://doi.org/10.1175/1520-0485(1985)015<1378:CAPOTN>2.0.CO;2)  
961 [0485\(1985\)015<1378:CAPOTN>2.0.CO;2](https://doi.org/10.1175/1520-0485(1985)015<1378:CAPOTN>2.0.CO;2), 1985.

962 Horvat, C.: Marginal ice zone fraction benchmarks sea ice climate model skill, *Nature*  
963 *communications*, 12, 2221, <https://doi.org/10.1038/s41467-021-22004-7>, 2021.

964 Horvat, C., Blanchard-Wrigglesworth, E., and Petty, A. A.: Observing waves in sea ice with  
965 ICESat-2. *Geophysical Research Letters*, 47, e2020GL087629.  
966 <https://doi.org/10.1029/2020GL087629>, 2020.



---

967 Horvat, C. and Tziperman, E.: A prognostic model of the sea-ice floe size and thickness  
968 distribution, *The Cryosphere*, 9, 2119–2134, <https://doi.org/10.5194/tc-9-2119-2015>,  
969 2015.

970 Horvat, C., Tziperman, E., and Campin, J.-M.: Interaction of sea ice floe size, ocean eddies,  
971 and sea ice melting, *Geophys. Res. Lett.*, 43, 8083-8090,  
972 <https://doi.org/10.1002/2016GL069742>, 2016.

973 Horvat, C., Roach, L. A., Tilling, R., Bitz, C. M., Fox-Kemper, B., Guider, C., Hill, K., Ridout,  
974 A., and Shepherd, A.: Estimating the sea ice floe size distribution using satellite altimetry:  
975 theory, climatology, and model comparison, *The Cryosphere*, 13, 2869-2885,  
976 <https://doi.org/10.5194/tc-13-2869-2019>, 2019.

977 Hunke, E. C. and Dukowicz, J. K.: An elastic-viscous-plastic model for sea ice dynamics. *J.*  
978 *Phys. Oceanogr.* 27, 1849–67, [https://doi.org/10.1175/1520-](https://doi.org/10.1175/1520-0485(1997)027<1849:AEVPMF>2.0.CO;2)  
979 [0485\(1997\)027<1849:AEVPMF>2.0.CO;2](https://doi.org/10.1175/1520-0485(1997)027<1849:AEVPMF>2.0.CO;2), 1997.

980 Josberger, E. G., and Martin, S.: A laboratory and theoretical study of the boundary layer  
981 adjacent to a vertical melting ice wall in salt water. *J. Fluid Mech.*, 111, 439-473,  
982 <https://doi.org/10.1017/S0022112081002450>, 1981.

983 Kirby, J. T., and Chen, T. M.: Surface waves on vertically sheared flows: approximate  
984 dispersion relations. *J. Geophys. Res.*, 94, 1013-1027,  
985 <https://doi.org/10.1029/JC094iC01p01013>, 1989.

986 Kohout, A., Williams, M. J., Dean, S. M., and Meylan, M.: Storm-induced sea-ice breakup and  
987 the implications for ice extent. *Nature*, 509(7502), 604-607.  
988 <https://doi.org/10.1038/nature13262>, 2014.

989 Komen, G. J., Hasselmann, S., and Hasselmann, K.: On the existence of a fully developed  
990 wind-sea spectrum, *J. Phys. Oceanogr.*, 14, 1271-1285, [https://doi.org/10.1175/1520-](https://doi.org/10.1175/1520-0485(1984)014<1271:OTEOAF>2.0.CO;2)  
991 [0485\(1984\)014<1271:OTEOAF>2.0.CO;2](https://doi.org/10.1175/1520-0485(1984)014<1271:OTEOAF>2.0.CO;2), 1984,

992 Kumar, N., Voulgaris, G., Warner, J. C., and Olabarrieta, M.: Implementation of the vortex  
993 force formalism in the coupled ocean-atmosphere-wave-sediment transport (COAWST)

---

994 modeling system for inner shelf and surf zone applications, *Ocean Modelling*, 47, 65-95,  
995 <https://doi.org/10.1016/j.ocemod.2012.01.003>, 2012.

996 Kwok, R.: Arctic sea ice thickness, volume, and multiyear ice coverage: Losses and coupled  
997 variability (1958–2018), *Environ. Res. Lett.*, 13, 105005, [https://doi.org/10.1088/1748-](https://doi.org/10.1088/1748-9326/aae3ec)  
998 [9326/aae3ec](https://doi.org/10.1088/1748-9326/aae3ec), 2018.

999 Langhorne, P. J., Squire, V. A., Fox, C., and Haskell, T. G.: Break-up of sea ice by ocean waves,  
1000 *Annals of Glaciology*, 27, 438–442. <https://doi.org/10.3189/S0260305500017869>, 1998.

1001 Leonard, B., and Mokhtari, S.: ULTRA-SHARP Non oscillatory Convection Schemes for  
1002 High-Speed Steady Multidimensional Flow. Technical Report. NASA, 1990.

1003 Li, Z., Wang, Z., Wang, Q., Xie, Fei., and Lu, P.: Laboratory study on parameterization of ice  
1004 floe melt rate at ice-air and ice-water interfaces. *Haiyang Xuebao*, 43(7), 162-172,  
1005 <https://doi.org/10.12284/hyxb2021115>, 2021. (in Chinese)

1006 Liang, X., Losch, M., Nerger, L., Mu, L., Yang, Q., and Liu, C.: Using sea surface temperature  
1007 observations to constrain upper ocean properties in an Arctic sea ice-ocean data  
1008 assimilation system, *Journal of Geophysical Research: Oceans*, 124,  
1009 <https://doi.org/10.1029/2019JC015073>, 2019.

1010 Lipscomb, W. H., Hunke, E. C., Maslowski, W., and Jakacki, J.: Ridging, strength, and stability  
1011 in high-resolution sea ice models. *J. Geophys. Res.*, 112, C03S91,  
1012 <https://doi.org/10.1029/2005JC003355>, 2007.

1013 Liu, Q., Babanin, A. V., Zieger, S., Young, I. R., and Guan, C.: Wind and Wave Climate in the  
1014 Arctic Ocean as Observed by Altimeters. *Journal of Climate* 29, 22, 7957-7975,  
1015 <https://doi.org/10.1175/JCLI-D-16-0219.1>, 2016.

1016 Longuet-Higgins, M. S. and Stewart, R. W.: Radiation stresses and mass transport in surface  
1017 gravity waves with application to ‘surf beats’, *J. Fluid Mech.*, 13, 481-504,  
1018 <https://doi.org/10.1017/S0022112062000877>, 1962.

- 
- 1019 Loose, B., McGillis, W. R., Perovich, D., Zappa, C. J., and Schlosser, P.: A parameter model of  
1020 gas exchange for the seasonal sea ice zone, *Ocean Sci.*, 10, 17-28,  
1021 <https://doi.org/10.5194/os-10-17-2014>, 2014.
- 1022 Liu, A. K., Holt, B., and Vachon, P. W.: Wave propagation in the marginal ice zone: Model  
1023 predictions and comparisons with buoy and synthetic aperture radar data, *J. Geophys. Res.*,  
1024 96(C3), 4605-4621, <https://doi.org/10.1029/90JC02267>, 1991.
- 1025 Liu, D., Tsarau, A., Guan, C., and Shen, H. H.: Comparison of ice and wind-wave modules in  
1026 WAVEWATCH III® in the Barents Sea, *Cold Regions Science and Technology*, 172,  
1027 103008, <https://doi.org/10.1016/j.coldregions.2020.103008>, 2020.
- 1028 Lu, P., Li, Z., Cheng, B., and Leppäranta, M.: A parameterization of the ice-ocean drag  
1029 coefficient, *J. Geophys. Res.*, 116, C07019, <https://doi.org/10.1029/2010JC006878>, 2011.
- 1030 Lukovich, J. V., Stroeve, J. C., Crawford, A., Hamilton, L., Tsamados, M., Heerton, H., and  
1031 Massonnet, F.: Summer Extreme Cyclone Impacts on Arctic Sea Ice, *Journal of Climate*,  
1032 34(12), 4817-4834, <https://doi.org/10.1175/JCLI-D-19-0925.1>, 2021.
- 1033 Madsen, O. S., Poon, Y.-K., and Graber, H. C.: Spectral wave attenuation by bottom friction:  
1034 Theory, *Proc. 21th Int. Conf. Coastal Engineering*, ASCE, 492-504,  
1035 <https://doi.org/10.1061/9780872626874.035>, 1988.
- 1036 Martin, T., Tsamados, M., Schroeder, D., and Feltham, D. L.: The impact of variable sea ice  
1037 roughness on changes in Arctic Ocean surface stress: A model study, *J. Geophys. Res.*  
1038 *Oceans*, 121, 1931–1952, <https://doi.org/10.1002/2015JC011186>, 2016.
- 1039 Maykut, G. A. and Perovich, D. K.: The role of shortwave radiation in the summer decay of a  
1040 sea ice cover, *J. Geophys. Res.-Ocean.*, 92, 7032–7044,  
1041 <https://doi.org/10.1029/JC092iC07p07032>, 1987.
- 1042 Maykut, G. A. and McPhee, M. G.: Solar heating of the Arctic mixed layer, *J. Geophys. Res.-*  
1043 *Oceans*, 100, 24691–24703, <http://doi.org/10.1029/95JC02554>, 1995.
- 1044 Meylan, M., and Squire, V. A.: The response of ice floes to ocean waves, *J. Geophys. Res.*,  
1045 99(C1), 891–900, <https://doi.org/10.1029/93JC02695>, 1994.

---

1046 Meylan, M. H., Bennetts, L. G., and A. L. Kohout: In situ measurements and analysis of ocean  
1047 waves in the Antarctic marginal ice zone, *Geophys. Res. Lett.*, 41, 1-6,  
1048 <https://doi.org/10.1002/2014GL060809>, 2014.

1049 Montiel, F., Squire, V., and Bennetts, L.: Attenuation and directional spreading of ocean wave  
1050 spectra in the marginal ice zone. *Journal of Fluid Mechanics*, 790, 492-522.  
1051 <https://doi.org/10.1017/jfm.2016.21>, 2016.

1052 Morrison, H., Thompson, G., and Tatarskii, V.: Impact of Cloud Microphysics on the  
1053 Development of Trailing Stratiform Precipitation in a Simulated Squall Line: Comparison  
1054 of One- and Two-Moment Schemes. *Mon. Wea. Rev.*, 137, 991-1007.  
1055 <https://doi.org/10.1175/2008MWR2556.1>, 2009.

1056 Nakanishi, M., and Niino, H.: Development of an improved turbulence closure model for the  
1057 atmospheric boundary layer. *J. Meteor. Soc. Japan*, 87, 895-912,  
1058 <https://doi.org/10.2151/jmsj.87.895>, 2009.

1059 Naughten, K. A., Galton-Fenzi, B. K., Meissner, K. J., England, M. H., Brassington, G. B.,  
1060 Colberg, F., Hattermann, T., and Debernard, J. B.: Spurious sea ice formation caused by  
1061 oscillatory ocean tracer advection schemes. *Ocean Model.*, 116, 108-117,  
1062 <https://doi.org/10.1016/j.ocemod.2017.06.010>, 2017.

1063 Nicolaus, M., Perovich, D., Spreen, G., Granskog, M., Albedyll, L., Angelopoulos, M., Anhaus,  
1064 P., Arndt, S., Belter, H., Bessonov, V., Birnbaum, G., Brauchle, J., Calmer, R.,  
1065 Cardellach, E., Cheng, B., Clemens-Sewall, D., Dacic, R., Damm, E., Boer, G., Demir,  
1066 O., Dethloff, K., Divine, D., Fong, A., Fons, S., Frey, M., Fuchs, N., Gabarró, C.,  
1067 Gerland, S., Goessling, H., Gradinger, R., Haapala, J., Haas, C., Hamilton, J., Hannula,  
1068 H.-R., Hendricks, S., Herber, A., Heuzé, C., Hoppmann, M., Høyland, K., Huntemann,  
1069 M., Hutchings, J., Hwang, B., Itkin, P., Jacobi, H.-W., Jaggi, M., Jutila, A., Kaleschke,  
1070 L., Katlein, C., Kolabutin, N., Krampe, D., Kristensen, S., Krumpfen, T., Kurtz, N.,  
1071 Lampert, A., Lange, B., Lei, R., Light, B., Linhardt, F., Liston, G., Loose, B., Macfarlane,  
1072 A., Mahmud, M., Matero, I., Maus, S., Morgenstern, A., Naderpour, R., Nandan, V.,

---

1073 Niubom, A., Oggier, M., Oppelt, N., Pätzold, F., Perron, C., Petrovsky, T., Pirazzini, R.,  
1074 Polashenski, C., Rabe, B., Raphael, I., Regnery, J., Rex, M., Ricker, R., Riemann-Campe,  
1075 K., Rinke, A., Rohde, J., Salganik, E., Scharien, R., Schiller, M., Schneebeli, M.,  
1076 Semmling, M., Shimanchuk, E., Shupe, M., Smith, M., Smolyanitsky, V., Sokolov, V.,  
1077 Stanton, T., Stroeve, J., Thielke, L., Timofeeva, A., Tonboe, R., Tavri, A., Tsamados,  
1078 M., Wagner, D., Watkins, D., Webster, M., and Wendisch, M.: Overview of the  
1079 MOSAiC expedition – Snow and Sea Ice, *Elementa Science of the Anthropocene*,  
1080 <https://doi.org/10.1525/elementa.2021.000046>, 2021.

1081 Notz, D., McPhee, M. G., Worster, M. G., Maykut, G. A., Schlünzen, K. H., and Eicken, H.:  
1082 Impact of underwater-ice evolution on Arctic summer sea ice, *J. Geophys. Res.-Oceans*,  
1083 108, 3223, <https://doi.org/10.1029/2001JC001173>, 2003.

1084 Notz, D., Jahn, A., Holland, M., Hunke, E., Massonnet, F., Stroeve, J., Tremblay, B., and  
1085 Vancoppenolle, M.: The CMIP6 Sea-Ice Model Intercomparison Project (SIMIP):  
1086 understanding sea ice through climate-model simulations, *Geosci. Model Dev.*, 9, 3427-  
1087 3446, <https://doi.org/10.5194/gmd-9-3427-2016>, 2016.

1088 Parkinson, C. L., and Comiso, J. C.: On the 2012 record low Arctic sea ice cover: Combined  
1089 impact of preconditioning and an August storm. *Geophysical Research Letters*, 40, 1356–  
1090 1361. <https://doi.org/10.1002/grl.50349>, 2013.

1091 Peng, L., Zhang, X., Kim, J.-H., Cho, K.-H., Kim, B.-M., Wang, Z., and Tang, H.: Role of  
1092 intense Arctic storm in accelerating summer sea ice melt: An in situ observational study.  
1093 *Geophysical Research Letters*, 48, e2021GL092714.  
1094 <https://doi.org/10.1029/2021GL092714>, 2021.

1095 Perovich, D.: On the summer decay of a sea ice cover, PhD thesis, University of Washington,  
1096 Seattle, 48–96, 1983.

1097 Perovich, D., Meier, W., Tshudi, M., Hendricks, S., Petty, A. A., Divine, D., Farrell, S., Gerland,  
1098 S., Haas, C., Kaleschke, L., Pavlova, O., Ricker, R., Tian-Kunze, X., Webster, M., and

---

1099 Wood, K.: Sea Ice, Arctic Report Card 2020, Thoman, R. L., Richter-Menge, J., and  
1100 Druckenmiller, M. L., Eds., <https://doi.org/10.25923/n170-9h57>, 2020.

1101 Rampal, P., Weiss, J., and Marsan, D.: Positive trend in the mean speed and deformation rate  
1102 of Arctic sea ice, 1979–2007, *J. Geophys. Res.*, 114, C05013,  
1103 <https://doi.org/10.1029/2008JC005066>, 2009.

1104 Roach, L. A., Horvat, C., Dean, S. M., and Bitz, C. M.: An emergent sea ice floe size  
1105 distribution in a global coupled ocean-sea ice model. *Journal of Geophysical Research:*  
1106 *Oceans*, 123, 4322–4337. <https://doi.org/10.1029/2017JC013692>, 2018a.

1107 Roach, L. A., Smith, M. M., and Dean, S. M.: Quantifying growth of pancake sea ice floes  
1108 using images from drifting buoys. *Journal of Geophysical Research: Ocean*, 123, 2851-  
1109 2866. <https://doi.org/10.1002/2017JC013693>, 2018b.

1110 Roach, L. A., Bitz, C. M., Horvat, C., and Dean, S. M.: Advances in Modeling Interactions  
1111 Between Sea Ice and Ocean Surface Waves, *J. Adv. Model. Earth Syst.*, 11, 4167-4181,  
1112 <https://doi.org/10.1029/2019MS001836>, 2019.

1113 Rogers, W. E., Meylan, M. H., and Kohout, A. L.: Frequency Distribution of Dissipation of  
1114 Energy of Ocean Waves by Sea Ice Using Data from Wave Array 3 of the ONR "Sea State"  
1115 Field Experiment. *NRL Report NRL/MR/7322–18-9801.*, 25 pp, Available from  
1116 <https://www7320.nrlssc.navy.mil/pubs.php>, 2018.

1117 Rogers, W. E.: Implementation of sea ice in the wave model SWAN, *NRL Memorandum Report*  
1118 *NRL/MR/7322–19-9874*, 25pp, Available from  
1119 <https://www7320.nrlssc.navy.mil/pubs.php>, 2019.

1120 Rothrock, D. A. and Thorndike, A. S.: Measuring the sea ice floe size distribution, *J. Geophys.*  
1121 *Res.*, 89, 6477–6486, <https://doi.org/10.1029/JC089iC04p06477>, 1984.

1122 Saha, S., Moorthi, S., Wu, X., Wang, J., Nadiga, S., Tripp, P., Behringer, D., Hou, Y., Chuang,  
1123 H., Iredell, M., Ek, M., Meng, J., Yang, R., Mendez, M. P., van den Dool, H., Zhang, Q.,  
1124 Wang, W., Chen, M., and Becker, E.: The NCEP climate forecast system version 2, *J.*  
1125 *Climate*, 27, 2185–2208, <https://doi.org/10.1175/JCLI-D-12-00823.1>, 2014.

---

1126 Schäfer, M., Bierwirth, E., Ehrlich, A., Jäkel, E., and Wendisch, M.: Airborne observations and  
1127 simulations of three-dimensional radiative interactions between Arctic boundary layer  
1128 clouds and ice floes, *Atmos. Chem. Phys.*, 15, 8147-8163, [https://doi.org/10.5194/acp-15-](https://doi.org/10.5194/acp-15-8147-2015)  
1129 [8147-2015](https://doi.org/10.5194/acp-15-8147-2015), 2015.

1130 Schmidt, G. A., Bitz, C. M., Mikolajewicz, U., and Tremblay, L.-B.: Ice–ocean boundary  
1131 conditions for coupled models, *Ocean Model.*, 7, 59-74, [https://doi.org/10.1016/S1463-](https://doi.org/10.1016/S1463-5003(03)00030-1)  
1132 [5003\(03\)00030-1](https://doi.org/10.1016/S1463-5003(03)00030-1), 2004.

1133 Sepp, M., and Jaagus, J.: Changes in the activity and tracks of Arctic cyclones. *Climatic Change*,  
1134 105(3), 577–595. <https://doi.org/10.1007/s10584-010-9893-7>, 2011.

1135 Shepetchkin, A. F., and McWilliams, J. C.: The Regional Ocean Modeling System: A split-  
1136 explicit, free-surface, topography following coordinates ocean model, *Ocean Modelling*,  
1137 9, 347-404, <https://doi.org/10.1016/j.ocemod.2004.08.002>, 2005.

1138 Simmonds, I., and Rudeva, I.: The great Arctic cyclone of August 2012, *Geophys. Res. Lett.*,  
1139 39, L23709, <https://doi.org/10.1029/2012GL054259>, 2012.

1140 Smith, M. M., Holland, M., and Light, B.: Arctic sea ice sensitivity to lateral melting  
1141 representation in a coupled climate model, *The Cryosphere*, 16, 419-434,  
1142 <https://doi.org/10.5194/tc-16-419-2022>, 2022.

1143 Spreen, G., Kwok, R., and Menemenlis, D.: Trends in Arctic sea ice drift and role of wind  
1144 forcing: 1992–2009, *Geophys. Res. Lett.*, 38, L19501,  
1145 <https://doi.org/10.1029/2011GL048970>, 2011.

1146 Squire, V. A.: Ocean Wave Interactions with Sea Ice: A Reappraisal, *Annual Review of Fluid*  
1147 *Mechanics*, 52:1, 37-60, <https://doi.org/10.1146/annurev-fluid-010719-060301>, 2020.

1148 Squire, V. A., and Montiel, F.: Evolution of Directional Wave Spectra in the Marginal Ice Zone:  
1149 A New Model Tested with Legacy Data. *Journal of Physical Oceanography* 46, 10, 3121-  
1150 3137, <https://doi.org/10.1175/JPO-D-16-0118.1>, 2016.

1151 Steele, M.: Sea ice melting and floe geometry in a simple ice-ocean model, *J. Geophys. Res.*,  
1152 97, 17-729-17738, <https://doi.org/10.1029/92JC01755>, 1992.

---

1153 Steele, M., Morison, J. H., and Untersteiner, N.: The partition of air-ice-ocean momentum  
1154 exchange as a function of ice concentration, floe size, and draft, *J. Geophys. Res.*, 94(C9),  
1155 12739-12750, <https://doi.org/10.1029/JC094iC09p12739>, 1989.

1156 Steer, A., Worby, A., and Heil, P.: Observed changes in sea-ice floe size distribution during  
1157 early summer in the western Weddell Sea, *Deep Sea Res., Part II*, 55, 933-942,  
1158 <https://doi.org/10.1016/j.dsr2.2007.12.016>, 2008.

1159 Stern, D., P, Doyle, J. D., Barton, N. P., Finocchio, P. M., Komaromi, W. A., & Metzger, E. J.:  
1160 The impact of an intense cyclone on short-term sea ice loss in a fully coupled atmosphere-  
1161 ocean-ice model. *Geophysical Research Letters*, 47, e2019GL085580.  
1162 <https://doi.org/10.1029/2019GL085580>, 2020.

1163 Stopa, J. E., Ardhuin, F., and Girard-Ardhuin, F.: Wave climate in the Arctic 1992-2014:  
1164 seasonality and trends, *The Cryosphere*, 10, 1605–1629, [https://doi.org/10.5194/tc-10-](https://doi.org/10.5194/tc-10-1605-2016)  
1165 [1605-2016](https://doi.org/10.5194/tc-10-1605-2016), 2016.

1166 Taylor, P. K., and Yelland, M. J.: The dependence of sea surface roughness on the height and  
1167 steepness of the waves. *Journal of Physical Oceanography* 31, 572-590,  
1168 [https://doi.org/10.1175/1520-0485\(2001\)031<0572:TDOSSR>2.0.CO;2](https://doi.org/10.1175/1520-0485(2001)031<0572:TDOSSR>2.0.CO;2), 2001.

1169 Thomson, J., and Rogers, W. E.: Swell and sea in the emerging Arctic Ocean, *Geophys. Res.*  
1170 *Lett.*, 41, 3136–3140, <https://doi.org/10.1002/2014GL059983>, 2014.

1171 Thorndike, A. S., Rothrock, D. A., Maykut, G. A., and Colony, R.: The thickness distribution  
1172 of sea ice, *J. Geophys. Res.*, 80, 4501, <https://doi.org/10.1029/JC080i033p04501>, 1975.

1173 Toyota, T., Takatsuji, S., and Nakayama, M.: Characteristics of sea ice floe size distribution in  
1174 the seasonal ice zone, *Geophys. Res. Lett.*, 33, L02616,  
1175 <https://doi.org/10.1029/2005GL024556>, 2006.

1176 Toyota, T., Haas, C., and Tamura, T.: Size distribution and shape properties of relatively small  
1177 sea-ice floes in the Antarctic marginal ice zone in late winter, *Deep Sea Res., Part II*, 58,  
1178 1182–1193, <https://doi.org/10.1016/j.dsr2.2010.10.034>, 2011.



---

1179 Tschudi, M. A., Stroeve, J. C., and Stewart, J. S.: Relating the age of Arctic sea ice to its  
1180 thickness, as measured during NASA's ICESat and IceBridge campaigns. *Remote Sensing*,  
1181 8(6), 457, 2016.

1182 Tsamados, M., Feltham, D. L., Schroeder, D., Flocco, D., Farrell, S. L., Kurtz, N., Laxon, S.  
1183 W., and Bacon, S.: Impact of Variable Atmospheric and Oceanic Form Drag on  
1184 Simulations of Arctic Sea Ice. *Journal of Physical Oceanography* 44, 5, 1329-1353,  
1185 <https://doi.org/10.1175/JPO-D-13-0215.1>, 2014.

1186 Tsamados, M., Feltham, D., Petty, A., Schroeder, D., Flocco, D.: Processes controlling surface,  
1187 bottom and lateral melt of Arctic sea ice in a state of the art sea ice model. *Phil. Trans. R.*  
1188 *Soc. A*, 373: 20140167. <https://doi.org/10.1098/rsta.2014.0167>, 2015.

1189 Uchiyama, Y., McWilliams, J. C., and Shchepetkin, A. F.: Wave–current interaction in an  
1190 oceanic circulation model with a vortex-force formalism: Application to the surf zone,  
1191 *Ocean Modelling*, 34, 1-2, 16-35, <https://doi.org/10.1016/j.ocemod.2010.04.002>, 2010.

1192 Umlauf, L. and Burchard, H.: A generic length-scale equation for geophysical turbulence  
1193 models, *J. Marine Res.*, 61, 235-265, <https://doi.org/10.1357/002224003322005087>, 2003.

1194 Valkonen, E., Cassano, J., and Cassano, E.: Arctic cyclones and their interactions with the  
1195 declining sea ice: A recent climatology. *Journal of Geophysical Research: Atmospheres*,  
1196 126, e2020JD034366. <https://doi.org/10.1029/2020JD034366>, 2021.

1197 Vella, D., and Wettlaufer, J. S.: Explaining the patterns formed by ice floe interactions, *J.*  
1198 *Geophys. Res.*, 113, C11011, <https://doi.org/10.1029/2008JC004781>, 2008.

1199 Wang, R., and Shen, H. H.: Gravity waves propagating into an ice-covered ocean: A  
1200 viscoelastic model, *J. Geophys. Res.*, 115, C06024,  
1201 <https://doi.org/10.1029/2009JC005591>, 2010.

1202 Warner, J. C., Armstrong, B., He, R., and Zambon, J.: Development of a coupled ocean-  
1203 atmosphere-wave-sediment transport (COAWST) modeling system. *Ocean Modell.* 35,  
1204 230–244, <https://doi.org/10.1016/j.ocemod.2010.07.010>, 2010.

- 1205 Waseda, T., Nose, T., Kodaira, T., Sasmal, K., and Webb, A.: Climatic trends of extreme wave  
1206 events caused by Arctic cyclones in the western Arctic Ocean. *Polar Science*, 27, 100625.  
1207 <https://doi.org/10.1016/j.polar.2020.100625>, 2021.
- 1208 Waseda, T., Webb, A., Sato, K., Inoue, J., Kohout, A., Penrose, B., and Penrose, S.: Correlated  
1209 Increase of High Ocean Waves and Winds in the Ice-Free Waters of the Arctic Ocean. *Sci*  
1210 *Rep* 8, 4489, <https://doi.org/10.1038/s41598-018-22500-9>, 2018.
- 1211 Weiss J. and Dansereau V.: Linking scales in sea ice mechanics. *Phil. Trans. R. Soc. A.*, 375,  
1212 20150352, <http://doi.org/10.1098/rsta.2015.0352>, 2017.
- 1213 Wenta, M., Herman, A.: Area-Averaged Surface Moisture Flux over Fragmented Sea Ice: Floe  
1214 Size Distribution Effects and the Associated Convection Structure within the Atmospheric  
1215 Boundary Layer. *Atmosphere*, 10, 654. <https://doi.org/10.3390/atmos10110654>, 2019.
- 1216 Wilchinsky, A. V., Feltham, D. L., and Hopkins, M. A.: Effect of shear rupture on aggregate  
1217 scale formation in sea ice, *J. Geophys. Res.*, 115, C10002,  
1218 <https://doi.org/10.1029/2009JC006043>, 2010.
- 1219 [Yang, C.-Y., Liu, J., and Xu, S.: Seasonal Arctic sea ice prediction using a newly developed](#)  
1220 [fully coupled regional model with the assimilation of satellite sea ice observations, \*J. Adv.\*](#)  
1221 [\*Model. Earth Sy.\*, 12, e2019MS001938, <https://doi.org/10.1029/2019MS001938>, 2020.](#)
- 1222 [Yang, C.-Y., Liu, J., and Chen, D.: An improved regional coupled modeling system for Arctic](#)  
1223 [sea ice simulation and prediction: a case study for 2018, \*Geosci. Model Dev.\*, 15, 1155–](#)  
1224 [1176, <https://doi.org/10.5194/gmd-15-1155-2022>, 2022.](#)
- 1225 Zahn, M., Akperov, M., Rinke, A., Feser, F., and Mokhov, I. I.: Trends of cyclone characteristics  
1226 in the Arctic and their patterns from different reanalysis data. *Journal of Geophysical*  
1227 *Research: Atmospheres*, 123, 2737–2751. <https://doi.org/10.1002/2017JD027439>, 2018.
- 1228 Zhang, F., Pang, X., Lei, R., Zhai, M., Zhao, X., and Cai, Q.: Arctic sea ice motion change and  
1229 response to atmospheric forcing between 1979 and 2019. *International Journal of*  
1230 *Climatology*, 42(3), 1854-1876. <https://doi.org/10.1002/joc.7340>, 2022

删除了: 2015

---

1232 Zhang, J., Lindsay, R., Schweiger, A., and Steele, M.: The impact of an intense summer cyclone  
1233 on 2012 Arctic sea ice retreat. *Geophysical Research Letters*, 40, 720-726.  
1234 <https://doi.org/10.1002/grl.50190>, 2013.

1235 Zhang, J., Schweiger, A., Steele, M., and Stern, H.: Sea ice floe size distribution in the marginal  
1236 ice zone: Theory and numerical experiments, *J. Geophys. Res. Oceans*, 120,  
1237 <https://doi.org/10.1002/2015JC010770>, 2015.

1238 Zhang, J., Stern, H., Hwang, B., Schweiger, A., Steele, M., Stark, M., Graber, H. C.: Modeling  
1239 the seasonal evolution of the Arctic sea ice floe size distribution. *Elementa: Science of the*  
1240 *Anthropocene*, 4, 000126, <https://doi.org/10.12952/journal.elementa.000126>, 2016.  
1241

1242 **7. Tables**

1243 Table 1 The summary of physic parameterizations used in all pan-Arctic simulations.

WRF physics	
Cumulus	Grell-Freitas (Freitas et al. 2018)
Microphysics	Morrison 2-moment (Morrison et al. 2009)
Longwave radiation	CAM spectral band scheme (Collins et al. 2004)
Shortwave radiation	CAM spectral band scheme (Collins et al. 2004)
Boundary layer	MYNN (Nakanishi and Niino, 2009)
Land surface	Unified Noah LSM (Chen and Dudhia, 2001)
ROMS physics	
Tracer advection	Upwind third-order horizontal advection (U3H; Shchepetkin, and McWilliams, 2005) Centered fourth-order vertical advection (C4V; Shchepetkin, and McWilliams, 2005)
Tracer vertical mixing	Generic Length-Scale scheme (Umlauf and Burchard, 2003)
CICE physics	
Ice dynamics	EVP (Hunke and Dukowicz, 1997)
Ice thermodynamics	Bitz and Lipscomb (1999)
Shortwave albedo	Delta-Eddington (Briegleb and Light, 2007)
SWAN physics	
Exponential wind growth	Komen et al. (1984)
Whitecapping	Komen et al. (1984)
Quadruplets	Hasselmann et al. (1985)
Depth-induced breaking	Battjes and Janssen (1978)
Bottom friction	Madsen et al. (1988)
Sea ice dissipation	Collins and Rogers (2017); Rogers (2019)

1244

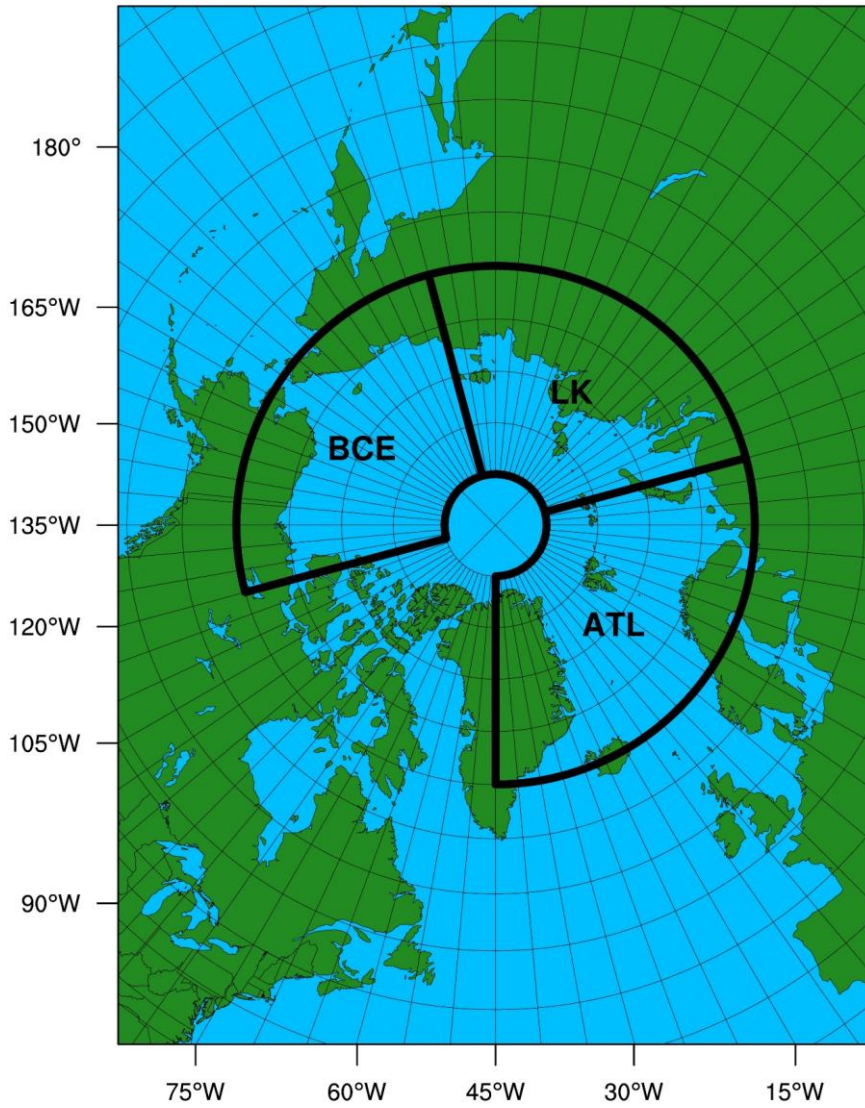
1245

1246 Table 2 The summary of the experiments conducted in this study and their main changes in the  
 1247 experiment design. MP87: Maykut and Perovich (1987). P83: Perovich (1983). M14: Meylan  
 1248 et al. (2014). R18: Rogers et al. (2018).

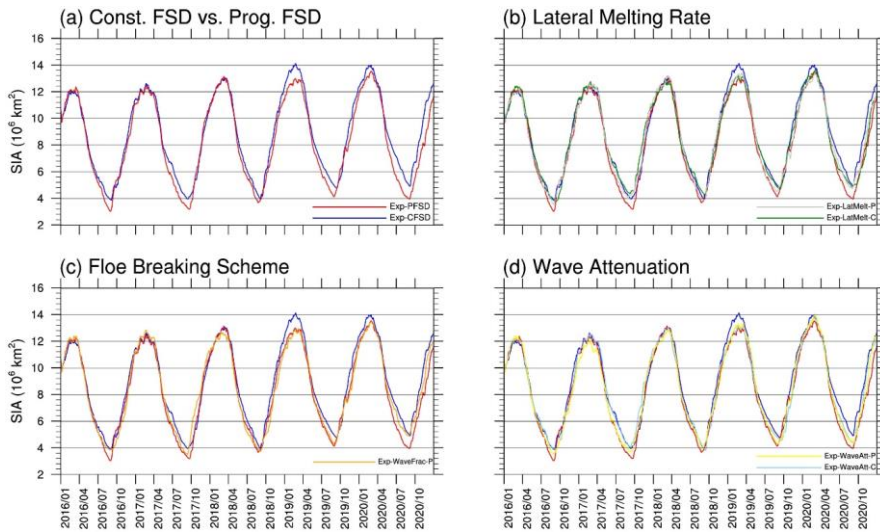
Experiment	Floe size	Lateral melting rate	Wave fracturing formulation	Wave attenuation coefficients
Exp-CFSD	Const. 300m	MP87	None	M14
Exp-PFSD	FSTD	MP87	Equally (PF1)	M14
Exp-LatMelt-C	Const. 300m	P83	None	M14
Exp-LatMelt-P	FSTD	P83	Equally (PF1)	M14
Exp-WaveFrac-P	FSTD	MP87	Bretschneider (PF2)	M14
Exp-WaveAtt-C	Const. 300m	MP87	None	R18
Exp-WaveAtt-P	FSTD	MP87	Equally (PF1)	R18

1249  
 1250

1251 **8. Figures**

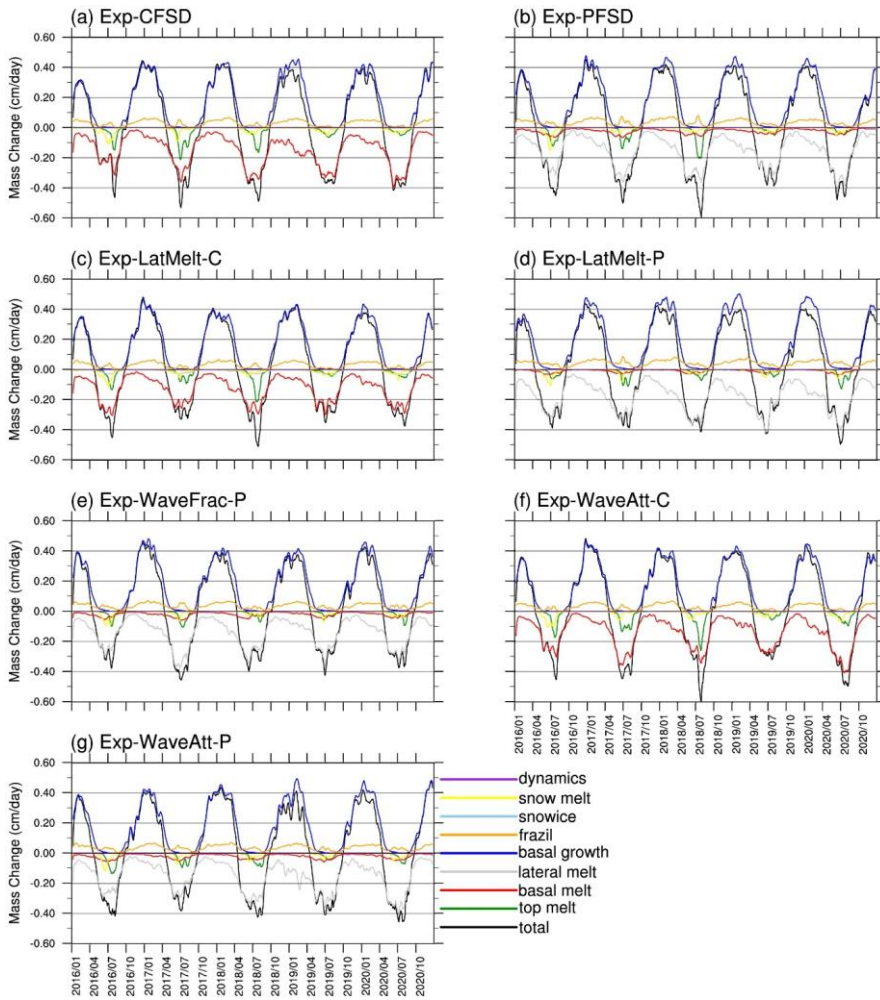


1252  
1253 Figure 1 The model domain used in CAPS for pan-Arctic sea ice simulations. Black boxes  
1254 indicate the subregions for analysis performed in this study.  
1255



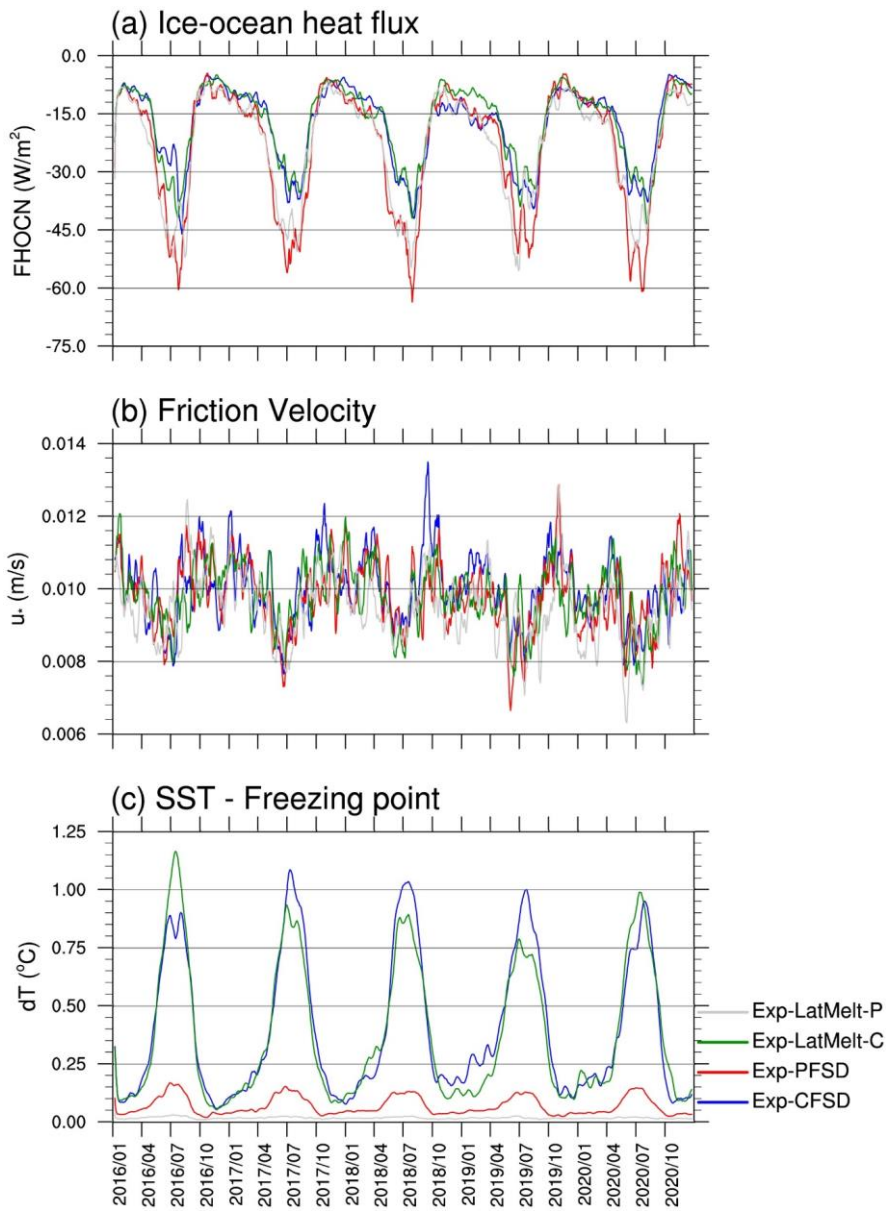
1256

1257 Figure 2 Time-series of Arctic sea ice area for Exp-CFSD (blue line), Exp-PFSD (red line),  
 1258 Exp-LatMelt-C (green line), Exp-LatMelt-P (grey line), Exp-WaveFrac-P (orange line), Exp-  
 1259 WaveAtt-C (light-blue line) and Exp-WaveAtt-P (yellow line).  
 1260



1261  
 1262 Figure 3 Time-series (15-day running-averaged) of sea ice mass budget terms for (a) Exp-  
 1263 CFSD, (b) Exp-PFSD, (c) Exp-LatMelt-C, (d) Exp-LatMelt-P, (e) Exp-WaveFrac-P, (f) Exp-  
 1264 WaveAtt-C, and (g) Exp-WaveAtt-P. Ice mass budget terms include: total mass change (black  
 1265 line), sea ice melt at the air-ice interface (top melt, green line), sea ice melt at the bottom of the  
 1266 ice (basal melt, red line), sea ice melt at the sides of the ice (lateral melt, grey line), sea ice  
 1267 growth at the bottom of the ice (basal growth, blue line), sea ice growth by supercooled open  
 1268 water (frazil, orange line), sea ice growth due to transformation of snow to sea ice (snowice,  
 1269 light-blue line), and sea ice mass change due to dynamics-related processes (dynamics, purple  
 1270 line) (Notz et al., 2016; Yang et al., 2022). For reference, snow melt term (yellow line) is  
 1271 included.





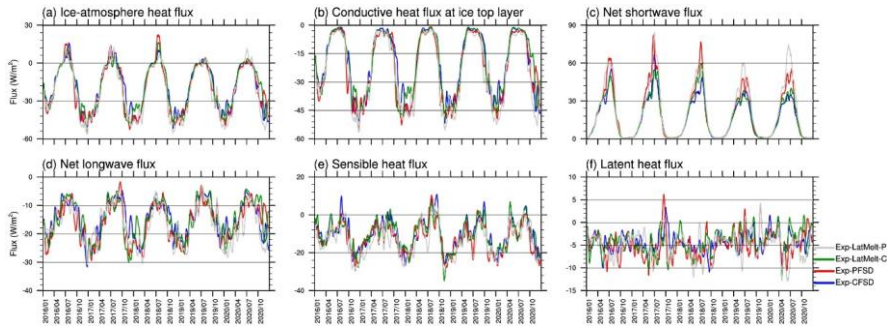
1272

1273 Figure 4 Time-series (15-day running-averaged) of (a) ice-ocean heat flux, (b) friction velocity

1274 at ice-ocean interface, and (c) the temperature difference between SST and freezing point for

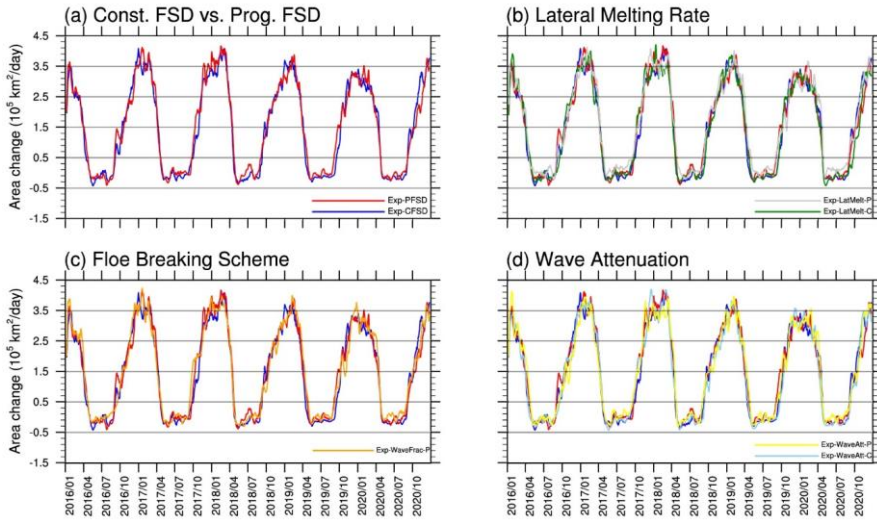
1275 Exp-CFSD (blue line), Exp-PFSD (red line), Exp-LatMelt-C (green line), and Exp-LatMelt-P

1276 (grey line). Note: (a) is positive downward and weighted by ice concentration.

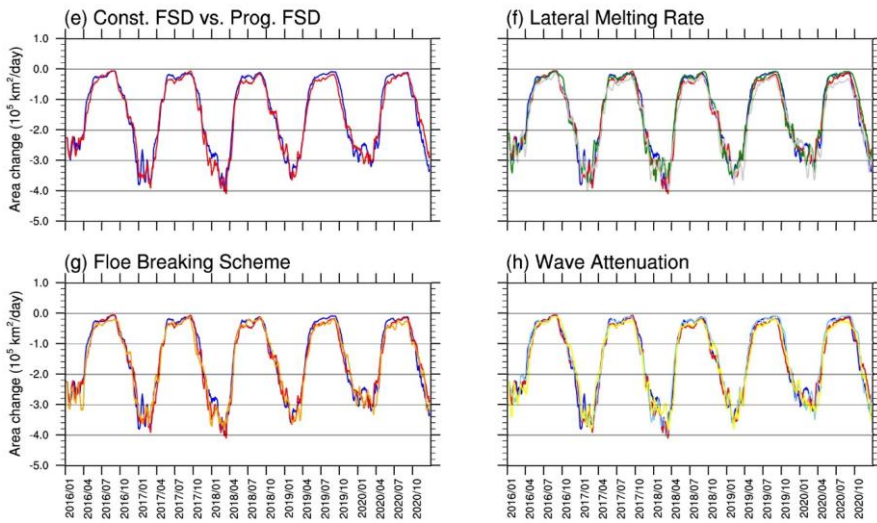


1277  
 1278 Figure 5 Time-series (15-day running-averaged) of (a) ice-atmosphere heat flux, (b) conductive  
 1279 heat flux at the ice top layer, (c) net shortwave flux, (d) net longwave flux, (e) sensible heat  
 1280 flux, and (f) latent heat flux for Exp-CFSD (blue line), Exp-PFSD (red line), Exp-LatMelt-C  
 1281 (green line), and Exp-LatMelt-P (grey line). Note: (a)-(e) are positive downwards and weighted  
 1282 by ice concentration.  
 1283

## Thermal Area Changes

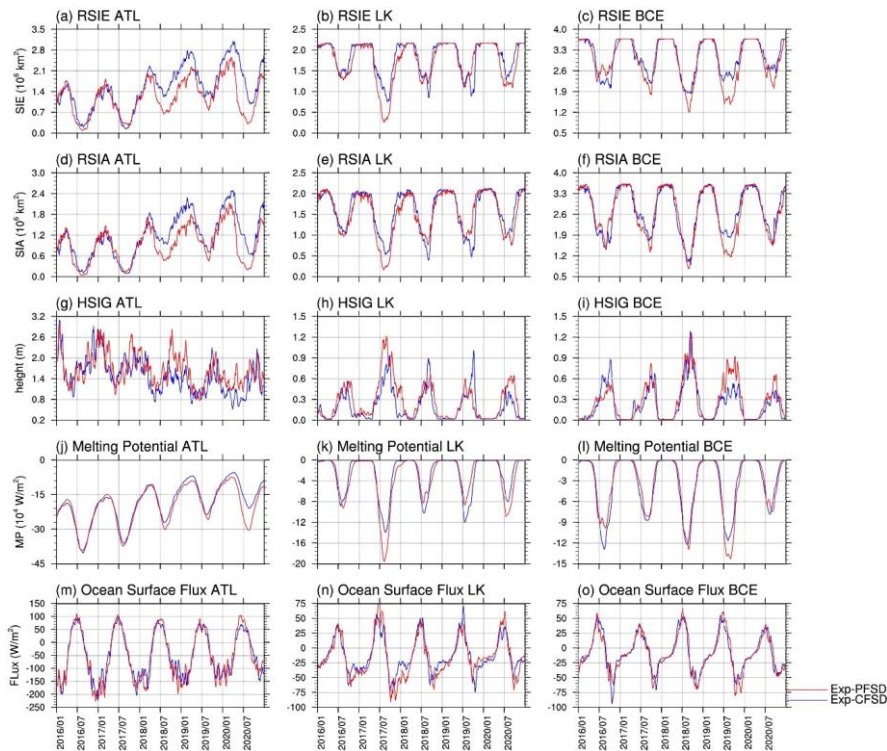


## Dynamical Area Changes



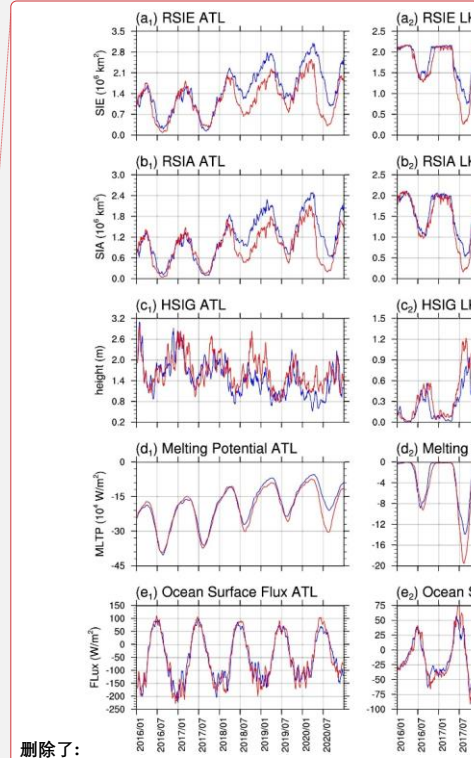
1284

1285 Figure 6 Time-series (15-day running-averaged) of sea ice area changes due to thermal  
 1286 processes (a-d, upper panel) and dynamical processes (e-h, bottom panel) for Exp-CFSD (blue  
 1287 line), Exp-PFSD (red line), Exp-LatMelt-C (green line), Exp-LatMelt-P (grey line), Exp-  
 1288 WaveFrac-P (orange line), Exp-WaveAtt-C (light-blue line) and Exp-WaveAtt-P (yellow line).



1289  
1290  
1291  
1292  
1293  
1294

Figure 7 Time-series of (a-c) ice extent, (d-f) ice area, (g-i) significant wave height, (j-l) melting potential, and (m-o) heat flux at the ocean surface in ATL, LK, and BCE regions for Exp-CFSD (blue line) and Exp-PFSD (red line). Note: significant wave height, melting potential, and heat flux at the ocean surface are region-averaged and 15-day running-averaged values.



删除了:

删除了: b

删除了: c

删除了: d

删除了: e

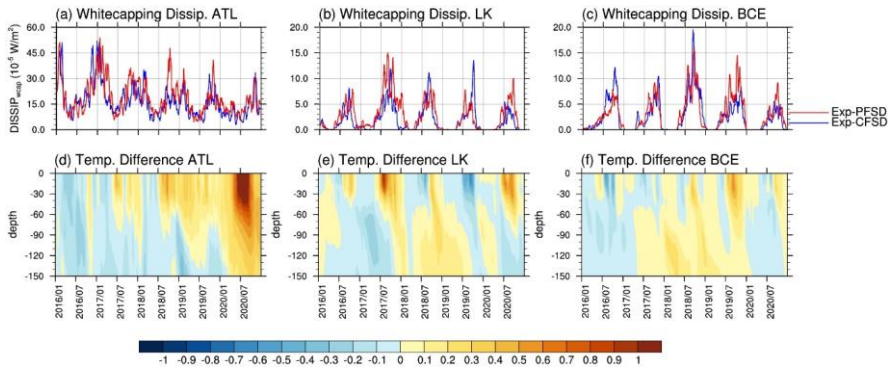
删除了: (1)

删除了: (2)

删除了: (3)

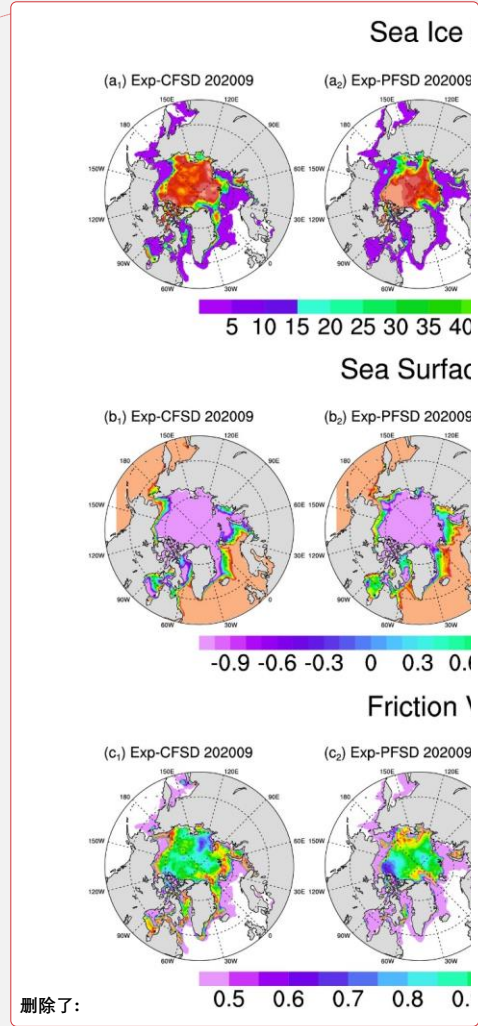
删除了: (c)-(e)

1304

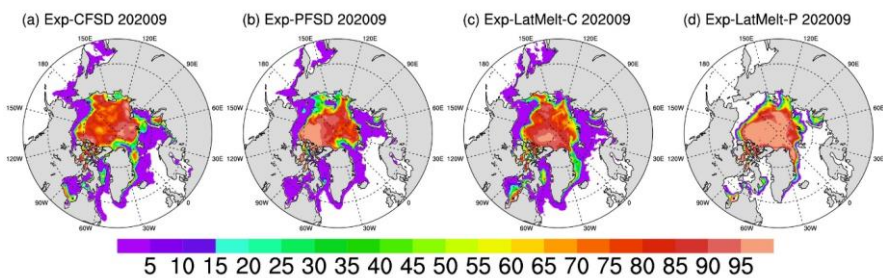


1305

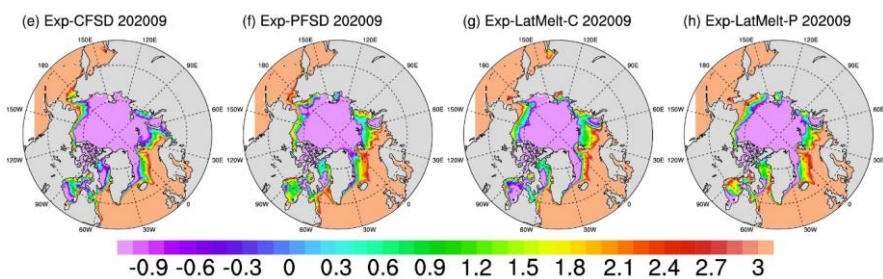
1306 Figure 8 Time-series (15-day running-averaged) of white capping dissipation averaged over (a)  
1307 ATL, (b) LK, and (c) BCE regions for Exp-CFSD (blue line) and Exp-PFSD (red line), and the  
1308 temperature profile difference between Exp-CFSD and Exp-PFSD in the upper 150 m averaged  
1309 over (d) ATL, (e) LK, and (f) BCE regions.  
1310



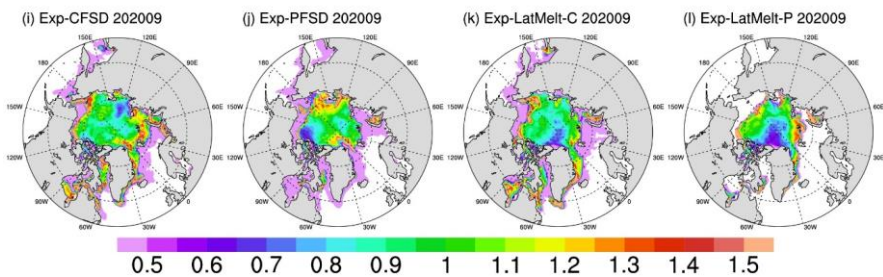
### Sea Ice Concentration (1)



### Sea Surface Temperature (°C)

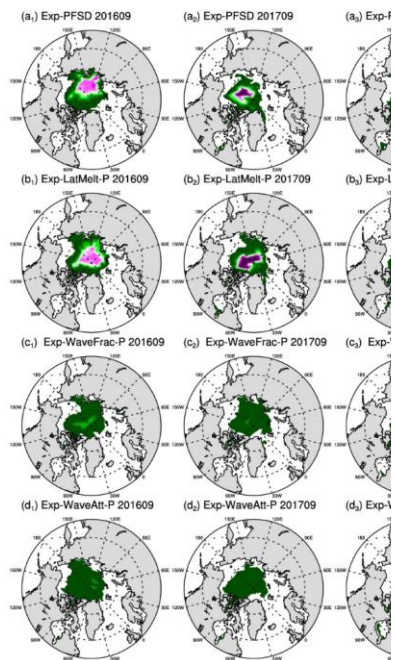
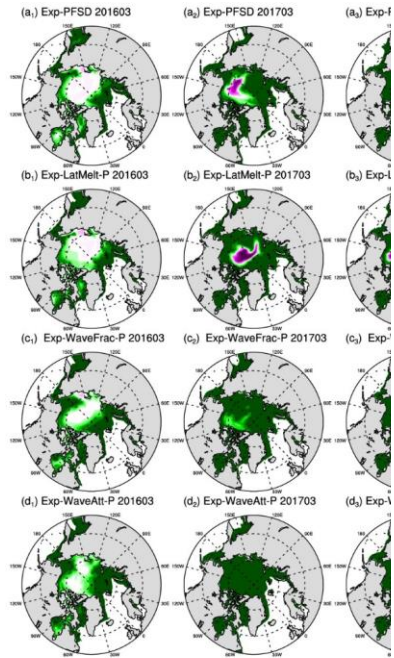
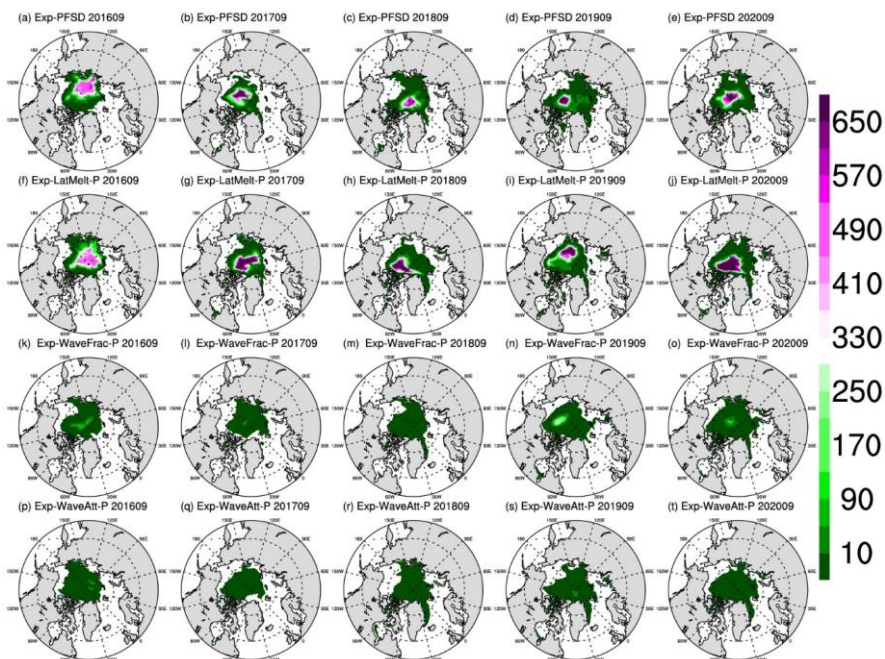
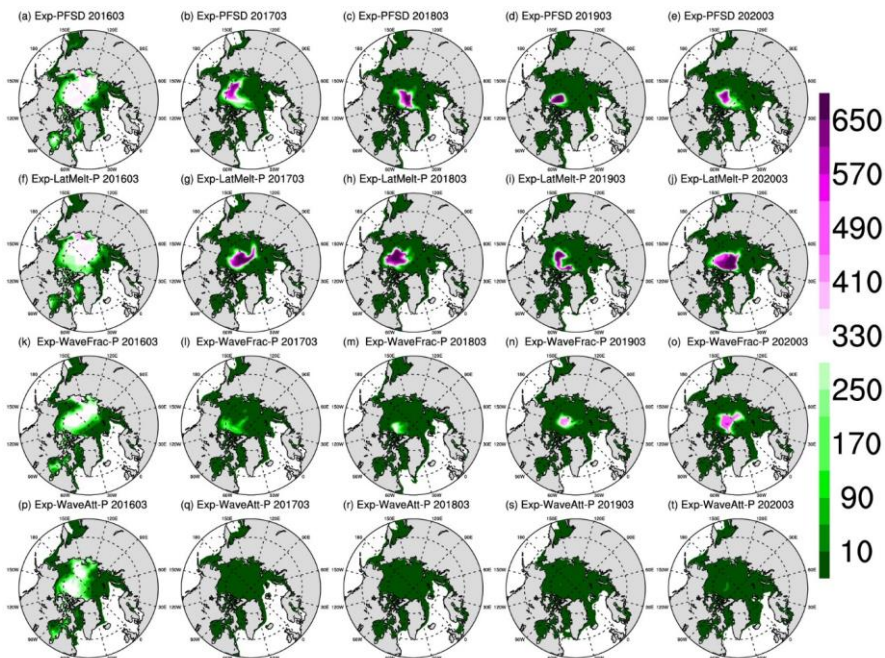


### Friction Velocity ( $10^{-3}$ m/s)



1313  
1314 Figure 9 The monthly-mean of (a-d) sea ice concentration, (e-h) sea surface temperature, and  
1315 (i-l) friction velocity in September 2020 for Exp-CFSD, Exp-PFSD, Exp-LatMelt-C, and Exp-  
1316 LatMelt-P.  
1317

- 删除了: b
- 带格式的: 两端对齐
- 删除了: c
- 删除了: .
- 删除了: (1)
- 删除了: (2)
- 删除了: (3)
- 删除了: (4)



删除了:

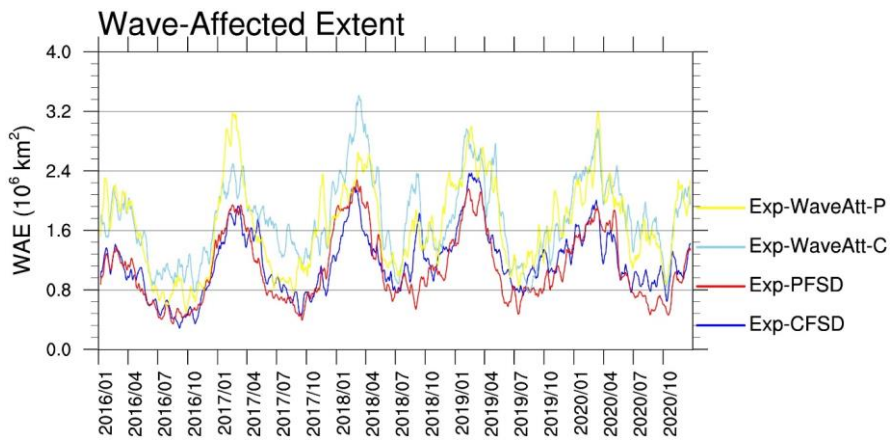


1328 Figure 10 The spatial distribution of the representative floe radius in March (upper panel) and  
1329 September (bottom panel) of (a-e) Exp-PFSD, (f-i) Exp-LatMelt-P, (k-o) Exp-WaveFrac-P, and  
1330 (p-t) Exp-WaveAtt-P for 2016-2020. Note: cells with less than 15% ice concentration are  
1331 treated as missing values.  
1332

删除了: b

删除了: c

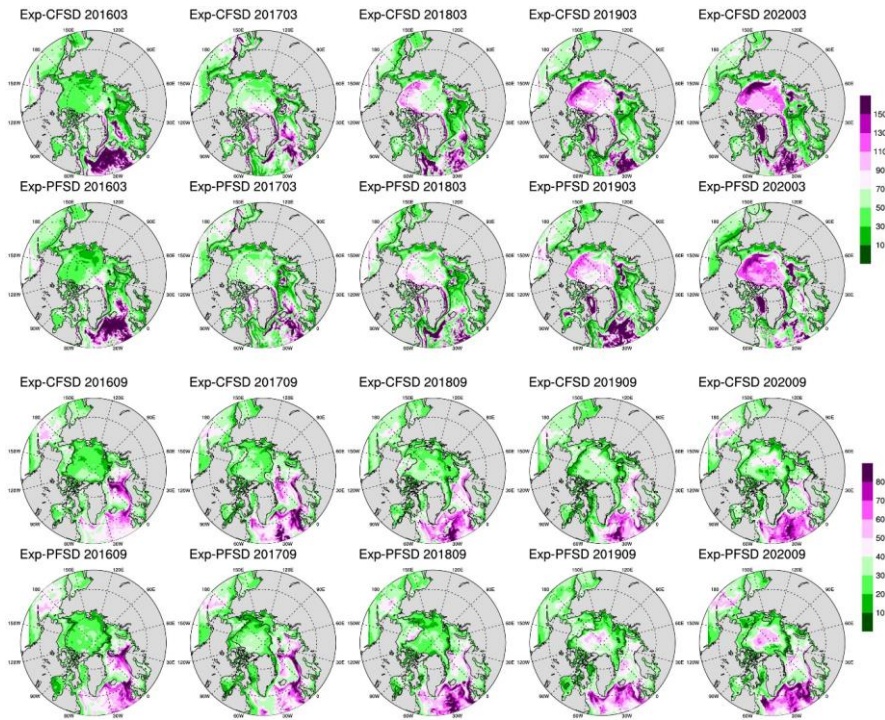
删除了: d



1336

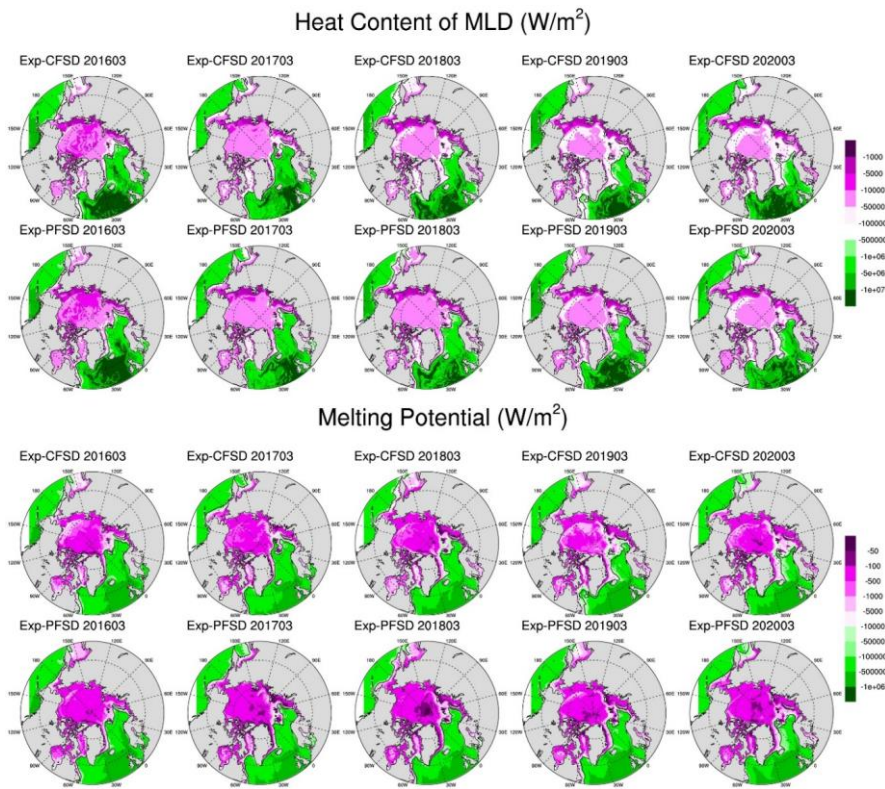
1337 Figure 11 Time-series (15-day running-averaged) of Arctic wave-affected extent for Exp-CFSD  
 1338 (blue line), Exp-PFSD (red line), Exp-WaveAtt-C (light-blue line) and Exp-WaveAtt-P (yellow  
 1339 line).

1340



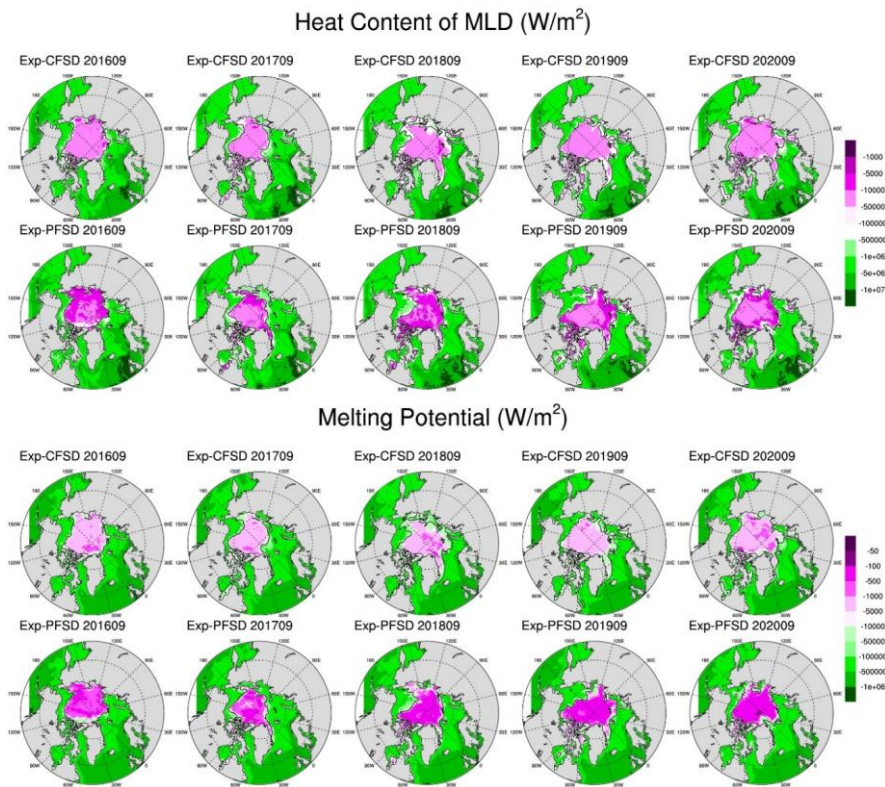
1341  
 1342  
 1343  
 1344  
 1345

Figure 12 Monthly mean of MLD in March (top panel) and September (bottom panel) of Exp-CFSD and Exp-PFSD for 2016-2020. Note: the black contour represents the average location of 15% ice concentration.



1346  
 1347  
 1348  
 1349  
 1350

Figure 13 March-averaged heat content of MLD (top panel) and melting potential (bottom panel) of Exp-CFSD and Exp-PFSD for 2016-2020. Note: the black contour represents the average location of 15% ice concentration.



1351

1352

Figure 14 Same as Figure 13, but for September-averaged values.